nature cancer

ARTICLES

https://doi.org/10.1038/s43018-021-00208-6

Check for updates

ULK1 inhibition overcomes compromised antigen presentation and restores antitumor immunity in *LKB1*-mutant lung cancer

Jiehui Deng[1], Aatish Thennavan[2], Igor Dolgalev[3], Ting Chen[1], Jie Li[3,4], Antonio Marzio[3,4], John T. Poirier[5], David H. Peng[1], Mirna Bulatovic[1], Subhadip Mukhopadhyay[6], Heather Silver[1], Eleni Papadopoulos[1], Val Pyon[1], Cassandra Thakurdin[1], Han Han[1], Fei Li[1], Shuai Li[1], Hailin Ding[1], Hai Hu[1], Yuanwang Pan[1], Vajira Weerasekara[7,8], Baishan Jiang[9,10], Eric S. Wang[9,10], Ian Ahearn[11], Mark Philips[11], Thales Papagiannakopoulos[3,12], Aristotelis Tsirigos[3], Eli Rothenberg[4], Justin Gainor[7], Gordon J. Freeman[13], Charles M. Rudin[14], Nathanael S. Gray[15], Peter S. Hammerman[13], Michele Pagano[3,4,16], John V. Heymach[17], Charles M. Perou[2], Nabeel Bardeesy[7,8] and Kwok-Kin Wong[1]✉

Inactivating mutations in *LKB1/STK11* are present in roughly 20% of nonsmall cell lung cancers (NSCLC) and portend poor response to anti-PD-1 immunotherapy. Unexpectedly, we found that *LKB1* deficiency correlated with elevated tumor mutational burden (TMB) in NSCLCs from nonsmokers and genetically engineered mouse models, despite the frequent association between high-TMB and anti-PD-1 treatment efficacy. However, *LKB1* deficiency also suppressed antigen processing and presentation, which are associated with compromised immunoproteasome activity and increased autophagic flux. Immunoproteasome activity and antigen presentation were restored by inhibiting autophagy through targeting the *ATG1/ULK1* pathway. Accordingly, ULK1 inhibition synergized with PD-1 antibody blockade, provoking effector T-cell expansion and tumor regression in *Lkb1*-mutant tumor models. This study reveals an interplay between the immunoproteasome and autophagic catabolism in antigen processing and immune recognition, and proposes the therapeutic potential of dual ULK1 and PD-1 inhibition in *LKB1*-mutant NSCLC as a strategy to enhance antigen presentation and to promote antitumor immunity.

LKB1-mutant NSCLC presents a clinical challenge, with notably worse overall outcomes compared to other NSCLC subsets and notable resistance to current immunotherapies as demonstrated in both patients and genetically engineered mouse models (GEMMs)[1–7]. *LKB1* is frequently comutated with *KRAS*[8] in NSCLC, and these tumors (designated KL) display an objective response rate to immune checkpoint inhibition of <10%, whereas *KRAS*/*TP53*-mutant NSCLC (designated KP) show a >30% objective response rate[1–4]. However, both KL and KP NSCLCs often arise in patients with a history of heavy smoking, which drives increased levels of nonsynonymous mutations, a feature that in NSCLC in general is associated with a more durable clinical response and better progression-free survival on checkpoint inhibitor treatment[8], likely due to the enhanced activation of neoantigen-specific $CD8^+$ T cells[9–11].

LKB1 mutation increases tumor mutational burden

Previous studies of human lung cancers not stratified by smoking status revealed comparably high tumour mutational burden (TMB) in KL and KP tumors. We used spontaneous *Kras*-driven NSCLCs arising in GEMMs[12] to more readily resolve the impact of *Lkb1* loss on TMB. We found that *Lkb1* comutation was associated with fivefold increase in TMB compared with *Trp53* comutation in both cell lines and lung nodules generated from GEMMs (Fig. 1a and Extended Data Fig. 1a). This effect was attributable to *Lkb1* status not *Trp53* status, since mouse cell lines with comutated *Lkb1*,

[1]Division of Hematology & Medical Oncology, Laura and Isaac Perlmutter Cancer Center, New York University Langone Medical Center, New York, NY, USA. [2]Lineberger Comprehensive Cancer Center, University of North Carolina, Chapel Hill, NC, USA. [3]Laura and Isaac Perlmutter Cancer Center, NYU Langone Medical Center, New York University, New York, NY, USA. [4]Department of Biochemistry and Molecular Pharmacology, New York University School of Medicine, New York, NY, USA. [5]Molecular Pharmacology Program, Memorial Sloan Kettering Cancer Center, New York, NY, USA. [6]Department of Radiation Oncology, Laura and Isaac Perlmutter Cancer Center, New York University School of Medicine, New York, NY, USA. [7]Center for Cancer Research, Massachusetts General Hospital, Boston, MA, USA. [8]Department of Medicine, Harvard Medical School, Boston, MA, USA. [9]Department of Cancer Biology, Dana-Farber Cancer Institute, Boston, MA, USA. [10]Department of Biological Chemistry and Molecular Pharmacology, Harvard Medical School, Boston, MA, USA. [11]Department of Medicine, Laura and Isaac Perlmutter Cancer Center, New York University School of Medicine, New York, NY, USA. [12]Department of Pathology, New York University School of Medicine, New York, NY, USA. [13]Department of Medical Oncology, Dana-Farber Cancer Institute, Harvard Medical School, Boston, MA, USA. [14]Memorial Sloan Kettering Cancer Center, New York, NY, USA. [15]Department of Chemical and Systems Biology, Chem-H and Stanford Cancer Institute, Stanford School of Medicine, Stanford University, Stanford, CA, USA. [16]Howard Hughes Medical Institute, New York University School of Medicine, New York, NY, USA. [17]Departments of Thoracic/Head and Neck Medical Oncology, The University of Texas MD Anderson Cancer Center, Houston, TX, USA. ✉e-mail: Kwok-Kin.Wong@nyulangone.org

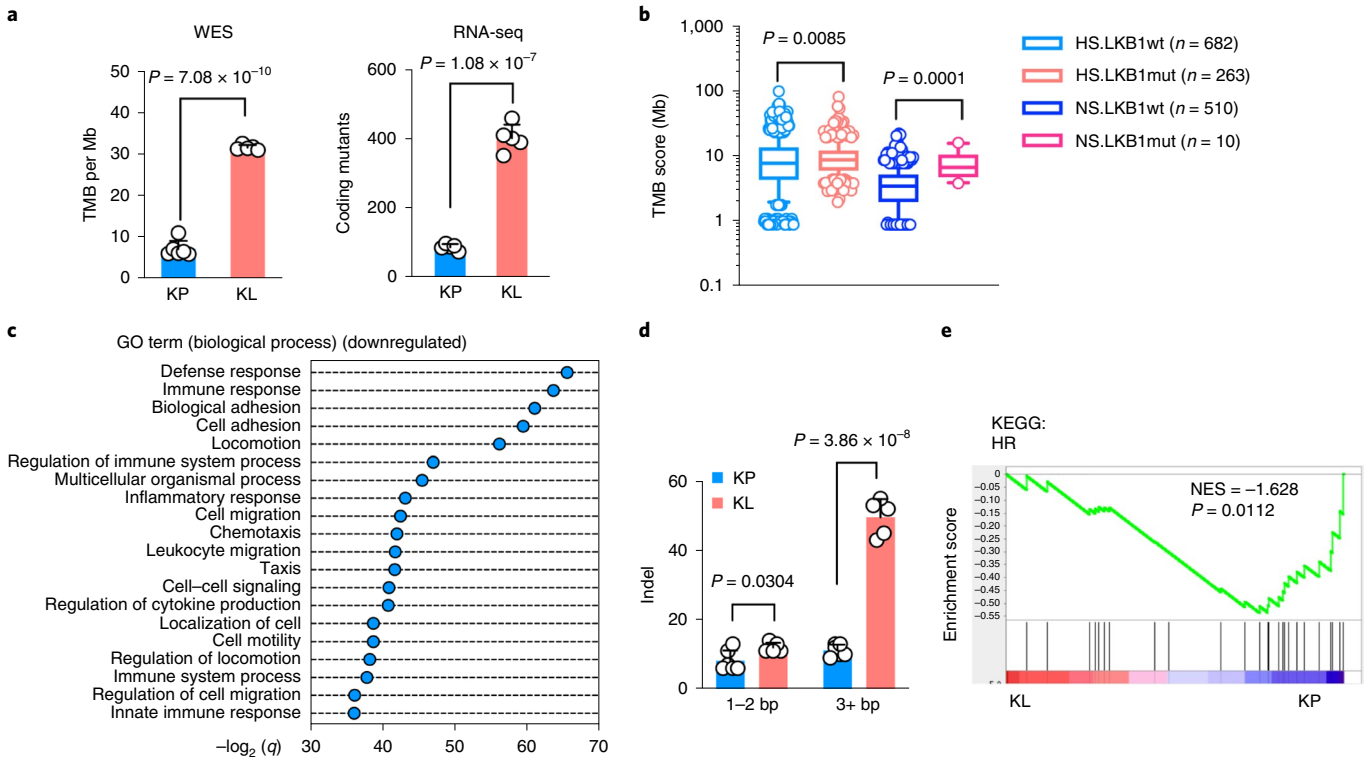

Fig. 1 | Increased TMB in *LKB1*-mutant NSCLC tumors. a, Comparison of TMB of nonsynonymous mutation using cell lines derived from $Kras^{G12D}Lkb1^{fl/fl}$ (KL) or $Kras^{G12D}Trp53^{fl/fl}$ (KP) NSCLC GEMMs lung nodules. Left panel, whole-exome sequencing (WES) of total nonsynonymous mutations per megabase (Mb) (KP, $n=6$ cell lines; KL $n=5$ cell lines) (mean ± s.d., two-sided Student's *t*-test). Right panel, RNA-seq for the total number coding region mutants of each cell line (KP $n=5$ cell lines; KL $n=5$ cell lines) (mean ± s.d., two-sided Student's *t*-test). **b**, TMB score from patients with NSCLC with or without *LKB1* mutation (HS.LKB1wt $n=682$; HS.LKB1mut $n=263$; NS.LKB1wt $n=510$; NS.LKB1mut $n=10$ patients each group: NS, never smoked; HS, heavy smoker) (Mann–Whitney test of $\log_{10}$-transformed TMB, two tailed. Boxes show the 25th to 75th percentiles with the line showing the median, and whiskers show the 10–90th percentiles. The Shapiro–Wilk test was used for normality test of transformed TMB score, two-tailed). **c**, Top suppressed biological process pathways from a patient with the TCGA *KRAS/LKB1* mutant compared with patients with the *KRAS/TP53* mutant. *x* axis, $-\log_2(q)$ value (Bonferroni) between the two groups (KP $n=22$, KL $n=19$ patients each group). **d**, Number of coding indel variants from either KP or KL cell lines of either short (1–2 basepairs (bp)) or long (≥3 bp) indels (KP $n=6$; KL $n=5$ cell lines each group) (mean ± s.d., unpaired two-sided multiple *t*-test, FDR < 0.05) **e**, GSEA of HR repair of KL and KP cells (KP $n=5$; KL $n=5$ cell lines each group).

Kras and *Trp53* (KLP) had comparable TMB to KL lines (Extended Data Figs. 1b,c). Similar to *LKB1*-mutant (LKB1mut) tumors from patients with cancer and KL GEMMs, KL cell lines generated from GEMMs showed a mixture of adenocarcinoma and squamous carcinomas phenotypes (Extended Data Fig. 1d).

Based on these findings in GEMMs, we analyzed a cohort of patients with NSCLC who had a known *LKB1* mutational status, smoking history and TMB measurement[13]. Notably, *LKB1* mutations in patients who had never smoked (NS.LKB1mut) were associated with a twofold increased TMB compared to a group who had never smoked with wildtype *LKB1* (NS.LKB1wt). TMB was comparable in *LKB1*-mutant (LKB1mut) and *LKB1*-wildtype (LKB1wt) NSCLCs in patients who were heavy smokers, who have a higher TMB in general[14] (Fig. 1b). As expected, both LKB1wt and LKB1mut heavy smoking groups had increased frequency of *KRAS* mutations compared to the groups who had never smoked. Furthermore, the *TP53* mutation percentage was higher in the LKB1wt group than the LKB1mut group for both patients who had never smoked and heavy smokers, consistent with previous studies (Extended Data Fig. 1e).

Despite suppressive immune response pathways in KL tumors (Fig. 1c and Extended Data Fig. 1f), KL tumors also had an increase in total number of coding insertion–deletions (indels) and nonsynonymous single-nucleotide variations (Fig. 1d and Extended Data Fig. 2a), although the percentage of indels among total nonsynonymous mutations was slightly decreased in KL (Extended Data Fig. 2b). Indels have been implicated in driving immunogenic responses due to the generation of immunogenic neoantigens[15,16]. *LKB1*-mutant NSCLCs show increases in COSMIC mutational signatures 20 and 26, which are associated with frequent small insertions and deletions[17]. Conversely, they show a decrease in signature 3, which suggests failure of DNA double-strand break (DSB) repair by homologous recombination (HR)[18], and signatures 7 and 22, which correlate with defective nucleotide excision repair[19] (Extended Data Fig. 2c,d). Consistent with increased nonsynonymous mutations, gene set enrichment analysis (GSEA) demonstrated the association between *LKB1* mutation and both the replication-dependent and -independent HR repair pathways (Fig. 1e and Extended Data Fig. 2e), but not other DNA repair-related pathways or others (Extended Data Fig. 2e,f). Collectively, these analyses suggest a link between *LKB1* inactivation and defective nucleotide excision repair and HR.

To quantify both HR and nonhomologous end joining repair (NHEJ) ratios in KL lines, we used a green fluorescent protein-(GFP-)based reporter system[20,21]. KL cells showed greatly suppressed HR and NHEJ compared with KP cell lines (Fig. 2a). KLP triple-mutant lung cancer cells also showed reduced HR but not NHEJ (Extended Data Fig. 3a). HR plays a dominant role during the late S/G2 and G1/early S cell cycle phases to repair DSBs and is typically nonmutagenic as compared with NHEJ[22,23]. HR

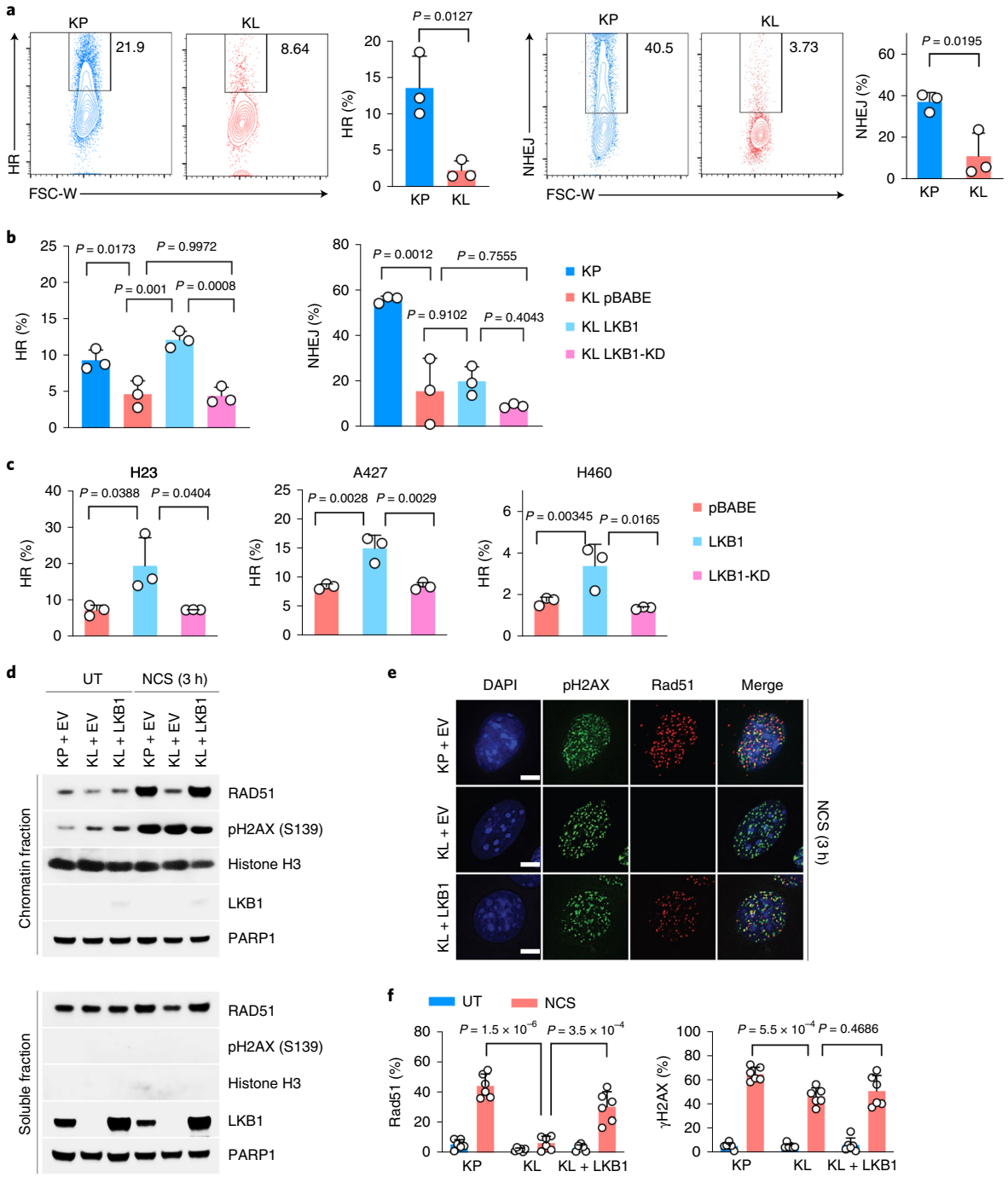

Fig. 2 | LKB1 is critical for maintaining HR during DNA DSB repair. a, Flow analysis of HR (left) and NHEJ (right) rate in both KP and KL cells through quantifying repaired HR or NHEJ reporter GFP$^+$ cells among total I-SceI expressing BFP$^+$ cells. Left, representative flow panels; right, quantification of HR (KP $n=3$; KL $n=3$ cell lines each group) or NHEJ (KP $n=3$; KL $n=3$ cell lines each group) percentage. Data are representative one of three independent experiments (mean ± s.d., two-tailed *t*-test, unpaired). **b**, Percentage of HR and NHEJ in KP and KL isogenic cells with wildtype or kinase-dead (KD) LKB1 overexpression. $n=3$ independent experiments for each group (mean ± s.d., two-tailed *t*-test, unpaired). **c**, HR ratio changes in human NSCLC *LKB1*-mutant cell lines H23, A427 and H460 with empty vector (pBABE), LKB1 or KLB1-KD overexpression. $n=3$ independent experiments for each group (mean ± s.d., two-tailed *t*-test, unpaired). **d**, Chromatin binding assay of either KP or KL cells with LKB1 overexpression after NCS induced DNA damage. Upper panel, chromatin fraction of bound proteins; lower panel, total soluble fraction of the proteins examined. Data represent one of two independent experiments. Blots are cropped and uncropped images can be found in the source data. **e**, Immunofluorescent staining of pH2AX and Rad51 foci at DNA DSB sites after NCS-induced damage in KP and KL cells with or without LKB1 overexpression. UT, untreated. NCS, NCS treated. Scale bars, 5 μm. Data are representative of three independent experiments. **f**, Quantification of Rad51 and pH2AX positive and negative cells as determined in **e** representative photos, and quantified as percentage among total cells. UT and NCS groups, KP $n=6$, KL $n=6$, KL + LKB1 $n=6$ independent experiments (mean ± s.d., two-tailed *t*-test, unpaired).

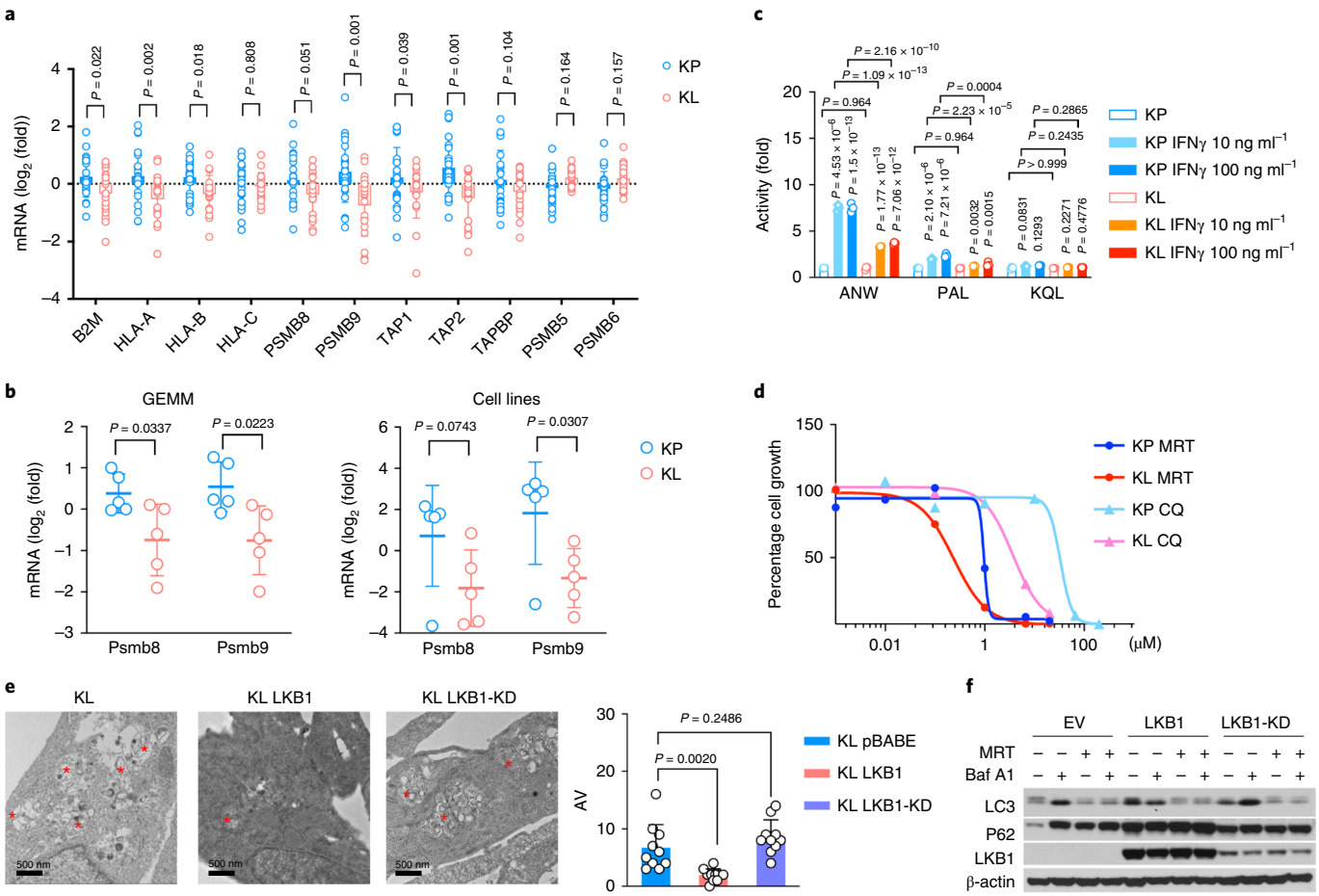

Fig. 3 | Suppressed antigen presentation machinery and immunoproteasome function in KL tumors. a, mRNA levels of antigen presentation related genes as well as conventional proteasome subunit expression from TCGA *KRAS/LKB1* mutant compared to patients with the *KRAS/TP53*-mutant NSCLC. KL $n=19$, KP $n=22$ patients (mean ± s.d., multiple two-tailed *t*-test, unpaired. FDR = 0.05). **b**, mRNA levels of immunoproteasome subunits *Lmp2/Psmb9* and *Lmp7/Psmb8* from KP and KL tumors either from GEMM (left) or cell lines (right). Left, KP $n=5$, KL $n=5$ lung nodules each group. Right, KP $n=5$, KL $n=5$ cell lines each group (mean ± s.d., multiple two-tailed *t*-test, unpaired. FDR = 0.05). **c**, Immunoproteasome subunits activity changes in *LKB1*-mutant tumors are measured by substrates Ac-ANW-AMC, Ac-PAL-AMC and Ac-KQL-AMC cleavage. The cleavage activities V_{max} were normalized with corresponding unstimulated samples and shown as fold changes. $n=3$ cell cultures for each group. Data shown are representative one of three independent experiments (mean ± s.d., multiple two-tailed *t*-test, unpaired, two-stage step-up method of Benjamini, Krieger and Yekutieli, FDR < 1%). **d**, Cell growth inhibition in KL and KP cells in response to autophagy inhibitors chloroquine (CQ) or ULK1 inhibitor MRT68921 (MRT). Data shown represent one of three independent experiments. $n=3$ cell cultures for each cell line with each treatment condition. **e**, Electron microscopy to visualize double-membraned autophagosome and autolysosome autophagic vacuole (AV) from KL, KL-LKB1 and KL-LKB1-KD cells. Top and left bottom, representative images. Data are representative of two independent experiments. * marked AV. Lower right, quantification of autophagic vacuole numbers for each cell line examined. Scale bar, 500 nm. For each group, $n=10$ fields. Each dot represents quantification of one random field of the electron microscopy image (mean ± s.d., two-tailed *t*-test, unpaired). **f**, Western blot showing autophagic flux by blocking lysosomal turnover with bafilomycin A1 (Baf A1) from KL-EV, KL-LKB1 and KL-LKB1(KD) cells. Data are representative of three independent experiments. Blots are cropped and uncropped images can be found in the source data.

was rescued by LKB1wt overexpression in KL lines, but not by kinase-dead *LKB1* (LKB1-KD) (Fig. 2b, left). By contrast, neither LKB1wt or LKB1-KD reconstitution restored NHEJ in *LKB1*-deficient cells (Fig. 2b, right). These data indicate that *LKB1* is important for maintaining homology directed repair but not NHEJ for DSBs. We further confirmed this phenomenon using human NSCLC cell lines. In particular, LKB1 overexpression increased HR, but not NHEJ levels, in the human *LKB1*-deficient lung cancer lines H23, A427 and H460 (Fig. 2c and Extended Data Fig. 3b). Thus, the increase in the HR signature in *LKB1*-deficient tumors correlates with a critical requirement for *LKB1* kinase activity for HR-mediated repair of DSBs, whereas the increase in NHEJ signatures is not directly related to LKB1 function.

On a DSB, PARP1 activity and a H2AX phosphorylation (pH2AX) signal can be detected at the DSB. This is followed by the recruitment of BRCA1 to promote DNA-end resection to generate single-strand DNA (ssDNA) for strand invasion and HR repair[22]. In turn, Rad51 recombinase is recruited at DSB sites to catalyze homology-dependent repair between a damaged DNA strand and an undamaged DNA template. To test acute DNA repair processes, we used the DNA damaging reagent neocarzinostatin (NCS) to induce both DSBs and ssDNA breaks. NCS treatment led to the expected induction of phosphorylation of H2AX-Ser139 in KP, KL and KL-LKB1 lines (Fig. 2d). However, the recruitment of Rad51 to chromatin was reduced specifically in KL cells and restored by LKB1 re-expression (Fig. 2d). Immunofluorescence staining

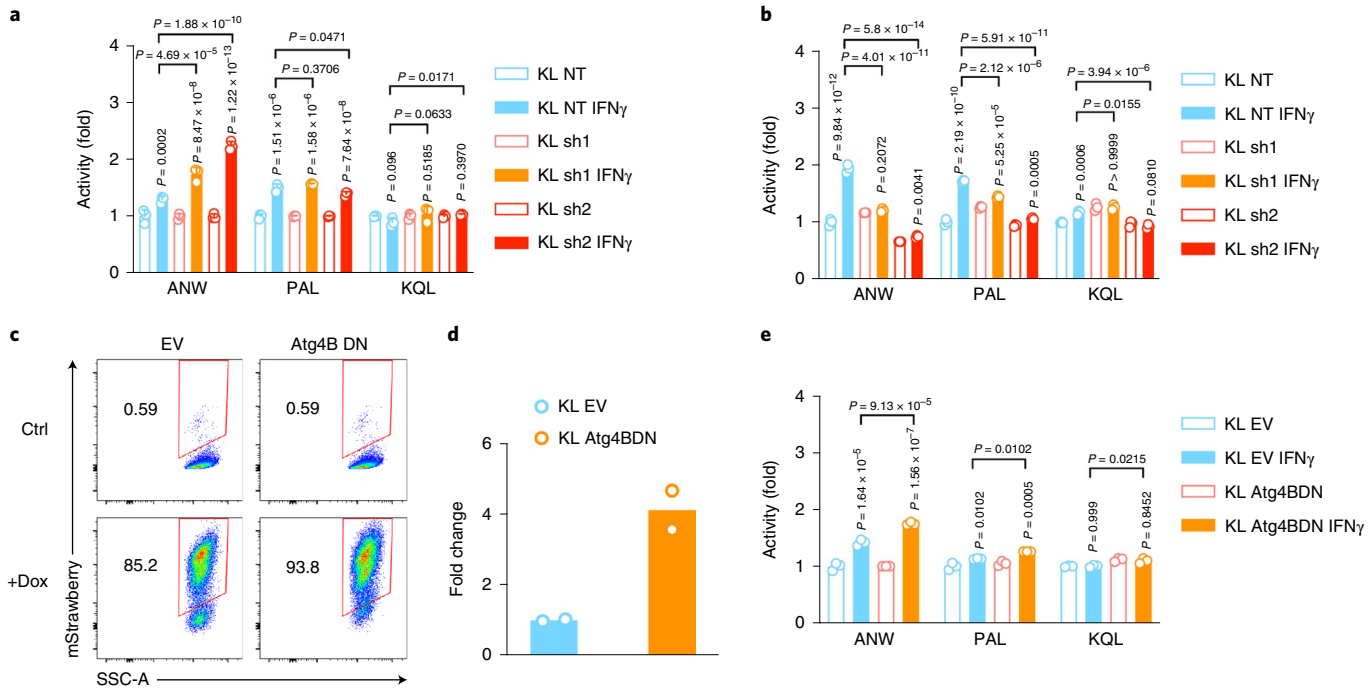

Fig. 4 | ULK1 as therapeutic target for *LKB1*-mutant tumors through inhibition autophagic flux. a,**b**, KL Ulk1 shRNA cell lines (**a**) and KP Ulk1 shRNA cell lines (**b**) were stimulated with IFN γ (10 ng ml^{-1}) for 24 h before the measurement of immunoproteasome activities showed as fold change of activities compared with untreated control. $n = 3$ independent experiments each group (mean ± s.d., unpaired *t*-test, two-tailed). Samples were either compared with none treated matching cells, or compared with a control (Ctrl) KL NT shRNA cell line after IFN*γ* stimulation as depicted. **c**, FACS analysis of mStrawberry signal on doxycycline treatment in KL-Atg4BDN cells generated. Data are representative of three independent experiments. **d**, Real-time PCR showing RNA level of Atga4B. $n = 2$ independent experiments each group. **e**, Immunoproteasome activity for KL stable cell lines with mStrawberry-Atg4BC74A overexpression (Atg4BDN). $n = 3$ independent cell cultures for each treatment group. Data shown are representative one of two independent experiments (mean ± s.d., multiple two-sided unpaired *t*-test, two-stage step-up method of Benjamini, Krieger and Yekutieli, statistics presented on top of each column is compared between IFNγ treatment with vehicle group of each cell line and pairwise comparisons between empty vector (EV) groups and Atg4BDN groups after IFNγ treatment are shown on top of the columns).

confirmed compromised in Rad51 recruitment to pH2AX foci in *LKB1*-deficient cells and rescue on LKB1 re-expression, despite comparable levels of pH2AX positivity (Fig. 2e,f and Extended Data Fig. 3c). Moreover, immunoprecipitation assays demonstrated the presence of LKB1 in a complex with BRCA1, but not to RAD51, AMPK or RPA, in response to NCS-induced damage (Extended Data Fig. 3d), suggesting that the functions of LKB1 in HR may involve complexing with BRCA1 with compromised RAD51 recruitment.

LKB1 loss suppresses antigen presentation

The relationship between DNA repair deficiency and immunotherapy response in the clinic is complex and incompletely understood. For example, while tumors with mismatch repair deficiency are more susceptible to immune checkpoint blockade[24], BRCA1 mutated tumors have suppressed antigen presentation and require additional immune stimulating agents to engender sensitivity to immunotherapy[25]. Pathway analysis from both The Cancer Genome Atlas (TCGA) and mouse cell-line datasets by gene set enrichments showed that *LKB1* mutations were associated with transcriptional signatures for suppressed immune response in cancer cells, including pathways involved in host defense response, immune response, regulation of immune system process, leukocyte activation and innate immune responses are suppressed in KL tumors compared with KP tumors (Fig. 1c, Extended Data Fig. 1f and Supplementary Table 1).

We reasoned that impaired neoantigen presentation by MHCI at the cell surface could function as a mechanism to promote immune evasion in the context of the HR defects and high TMB that are present in LKB1mut NSCLC. We found that patients with KL NSCLC have a decreased expression of the machinery for neoantigen processing and presentation, with reduced mRNA levels of *B2M*, *HLA-A*, *HLA-B*, *TAP1* and immunoproteasome subunit *PSMB9* compared to KP tumors (Fig. 3a and Extended Data Fig. 4a). By contrast, no differences were observed in the expression of the catalytic subunits of conventional proteasomal *PSMB5* and *PSMB6* (Fig. 3a). Similarly, KL mouse cancer cell lines and GEMM lung tumor nodules exhibited decreased expression of the immunoproteasome subunits *Psmb8* and *Psmb9* at the mRNA levels (Fig. 3b) and protein levels (Extended Data Fig. 4b) compared to murine KP tumors. TAP1 and Tapasin protein levels were reduced, where PSMB5 and PSMB6 were at comparable or increased levels in KL tumors (Extended Data Fig. 4b).

IFNγ stimulation induces the activity of the immunoproteasome subunits LMP7/PSMB8 (Ac-ANW) and LMP2/PSMB9 (Ac-PAL) along with upregulating the mRNA expression of classical class I MHC genes and processing factors, including *HLA-A*, *HLA-B*, *HLA-C*, *TAP1* and *TAPASIN*[26–29]. Notably, IFNγ-induced PSMB8 and PSMB9 activity was greatly attenuated in KL cells compared to KP cells, whereas there was no compromise in these transcriptional changes (Fig. 3c and Extended Data Fig. 4b). The impairment in PSMB8 and PSMB9 activity was specifically due to LKB1 loss, since KLP cells showed comparable levels to KL cells (Extended Data Fig. 4c,d) and since wildtype LKB1 reconstitution increased immunoproteasome activity in KL cells (Extended Data Fig. 4e). Finally, while we observed decreased cell surface MHCI expression in KL tumors in vivo, MHCI levels were comparably induced on

IFNγ stimulation in vitro (Extended Data Fig. 5a–c). Thus, uptake of the MHCI complex from the endoplasmic reticulum to the cell surface remains functional in *LKB1*-mutant tumors, whereas there is compromised generation of immunogenic peptides through the immunoproteasome.

Autophagy inhibition enhances immunoproteasome activity

Suppressed antigen processing for MHCI presentation could promote immune evasion in *LKB1*-deficient tumors. Hence, therapeutic strategies that increase antigen presentation might restore antitumor immunity and compensate for *LKB1* loss. Autophagy and proteasomal degradation are the two main pathways for quality control of cellular protein homeostasis, and reduced proteasome activity can induce autophagy as a compensatory process[30]. Notably, *KRAS*-mutant cancers, including those with LKB1 comutations, have been shown to depend on autophagy-lysosomal catabolism for tumor growth via both cell-autonomous and non-autonomous mechanism[31–34]. GSEA comparison of lung cancers from the GEMMs showed enrichment of autophagy pathways in the KL tumors compared to KP tumors (Extended Data Fig. 2e,f). Although there was also a trend toward enrichment in human KL lung tumors, it did not reach statistical significance, possibly due to interference of other comutations in patient tumors (Extended Data Fig. 2e,f). Unfolded protein pathways (UPR), which have been linked to autophagy and MHCI expression[35,36], did not show consistent differences in human and murine KL tumors (Extended Data Fig. 2e,f), indicating that UPR may not play a major role in antigen presentation defects resulting from of LKB1 inactivation.

Consistent with increased activity of the autophagy-lysosomal catabolic system in KL tumors and its requirement for in vitro proliferation[34], KL cells showed elevated sensitivity to autophagy inhibitors chloroquine and MRT68921 (Fig. 3d), which inhibit lysosomal acidification and ULK1/ULK2 kinase activity, respectively[37,38], compared to KP tumors. Using transmission electron microscopy (TEM) to quantify the number of autophagic vacuoles in KL cells, we found that reconstitution of LKB1, but not LKB1-KD, suppressed the number of autophagic vacuoles (Fig. 3e), consistent with increased autophagic catabolism in the absence of LKB1. Accordingly, inhibition of autolysosome acidification with bafilomycin A1 promoted accumulation of p62 and LC3II levels during nutrient deprivation (Earle's balanced salt solution, EBSS) in both KL-EV and KL-LKB1-KD cells, but not in KL cells expressing LKB1wt (Fig. 3f), in line with an increase in autophagic flux on LKB1 deficiency. MRT68921 treatment of KL cells increased levels of H-2D but not H-2K (Extended Data Fig. 5c). Moreover, PSMB8 activity was increased by *Ulk1* inhibition, as demonstrated by cleavage of Ac-ANW substrate (Fig. 4a,b and Extended Data Fig. 4c), providing evidence that targeting autophagy restores antigen presentation in *LKB1*-mutant cancers.

The block in autophagy caused by MRT68921 has been reported to involve targeting of ULK1 specifically, and not ULK2 (ref. [38]). Using a tandem fluorescent reporter of autophagic flux (GFP-RFP-LC3)[39] (Extended Data Fig. 6a,b), we confirmed that either short-hairpin RNA-mediated knockdown of *Ulk1* or MRT68921 treatment reduced autophagic flux in KL cells (Extended Data Fig. 6b–d). MRT68921 can also target TBK1 (ref. [38]), which has been implicated in LKB1-mediated immune suppression through the TBK1/STING pathway[40]. However, we found that MRT68921 treatment increased TBK1 activity, as reflected by pTBK1 levels, in LKB1 isogenic lines of human NSCLC, probably due to the immune stimulating effects of ULK1 inhibition (Extended Data Fig. 6e). Furthermore, inhibition key autophagy regulators downstream of ULK1—including Atg7, Atg13 and Atg4—caused similar effects of increases in antigen processing via enhanced immunoproteasome activity (Fig. 4c–e and Extended Data Fig. 6f–i).

ULK1 inhibition restores antitumor immunity in KL

Following our in vitro observations that KL cells are sensitive to ULK1 inhibition, and that targeting ULK1 restores antigen presentation with increased immunoproteasome activity, we sought to examine whether these effects translate to differential immune responses in vivo in *LKB1*-mutant and *LKB1*-wildtype cancer models. We confirmed that MRT68921 treatment blocked autophagic flux in KL lung tumors (Fig. 5a,b and Extended Data Fig. 7a,b). This led to increases in immunoproteasome activity (Fig. 5c–e and Extended Data Fig. 7c). MRT68921 treatment did not result in major toxicity (Extended Data Fig. 7d), and increased infiltration of both $CD4^+$ and $CD8^+$ T cells among total $CD45^+$ immune cells in the tumor-bearing lungs (Fig. 5f,g and Extended Data Fig. 8a–c). MRT68921 treatment alone did not result in an antitumor effect (Fig. 6a and Extended Data Fig. 7e). Anti-PD-1 antibody mono-therapy had modest and inconsistent tumor responses. Conversely, combination MRT68921 treatment enhanced the efficacy of anti-PD-1 therapy, with evident tumor regression in eight out of 15 tumors (Fig. 6a and Extended Data Fig. 7e). We observed similar increased immunoproteasome activity in KL tumors treated with another autophagy inhibitor chloroquine (CQ) (Fig. 5e). By contrast, KP tumors did not respond to either MRT68921 or PD-1 treatment alone or in combination (Extended Data Fig. 7f). Neutralizing antibodies against $CD8^+$ T cells blocked the effects of MRT68921 plus PD-1 combinational treatment on antitumor immunity in *LKB1*-mutant tumors (Fig. 6b), confirming that the efficacy of the combination involves $CD8^+$ cytotoxic T cells activation rather than tumor intrinsic effects. Combination treatment resulted in an increased $CD44^+$ $CD62L^-$ population within tumor infiltrating $CD8^+$ T cells (Fig. 6c, upper panels). The IL-7Rα subunit CD127 was reduced, while CD69, CCR7 and 2B4 levels did not change after treatment (Fig. 6c, lower panels, and Extended Data Fig. 8d). CD127 is reported to be critical for $CD8^+$ T cell homeostasis,

Fig. 5 | Targeting ULK1 increases immunoproteasome activity and T cell activity in vivo. a, Representative immunofluorescence image lung tumors of KL cells transduced with autophagy flux reporter GFP–LC3–RFP (GLR) after MRT68921 + PD-1 treatment. Data are representative of three independent experiments. Scale bar, 50 μm. **b**, Quantification of autophagic flux inhibition shown as GFP/RFP ratio for each immunofluorescence image after MRT68921 treatment. $n = 7$ fields from independent tumors each group. Data represent one of three independent experiments (data are presented as mean ± s.d., one-way ANOVA). **c**, Western blot shows antigen presentation related proteins, including PSMB9 and PSMB8, TAP1, Tapasin and B2M expression levels from KL lung nodules after MRT + PD-1 treatment. Each lane represents one lung nodule sample from individual mice of indicated groups. Blots are cropped and uncropped images can be found in the source data. **d**, Immunoproteasome activities of lung nodules from KL tumors after the treatment with MRT + PD-1. Showed as fold change of activities compared with vehicle control group. Vehicle, MRT, PD-1, $n = 6$ each group; MRT + PD-1 $n = 8$ individual tumor nodules from each group (mean ± s.d., one-way ANOVA). **e**, Immunoproteasome activities of lung nodules from KL allograft tumors nodules after the treatment with CQ + PD-1. Showed as fold change of activities compared with vehicle control group. $n = 6$ individual tumor nodules from each group (mean ± s.d., one-way ANOVA). **f**, Representative immunohistochemistry images of KL lung tumors treated with indicated treatment before staining (H&E) with $CD3^+$, $CD4^+$ and $CD8^+$ T lymphocyte infiltration in the lung. Data are representative of three independent experiments. Scale bar, 100 μm. **g**, Quantification of immune infiltrates shown in **f**. Veh $n = 7$, PD-1 $n = 5$, MRT $n = 5$, MRT + PD-1 $n = 10$ fields from independent tumors. Data are representative of two independent experiments (mean ± s.d., one-way ANOVA).

and T cell receptor engagement downregulates CD127 expression[41]. We also observed enhanced cytotoxicity, with increased levels of both CD107a and granzyme B after combination treatment group (Fig. 6d) as well as an increased ratio of CD8/Treg cells (Extended Data Fig. 8c). These data highlight increased CD8$^+$ cytotoxicity on engagement of T cell receptors with tumor-derived neoantigens, with suppressed cell death through CD127 inhibition.

In summary, we discovered that LKB1 loss of function leads to DNA DSB repair deficiency with suppressed HR repair, which results in increased TMB in patients with cancer. However, despite

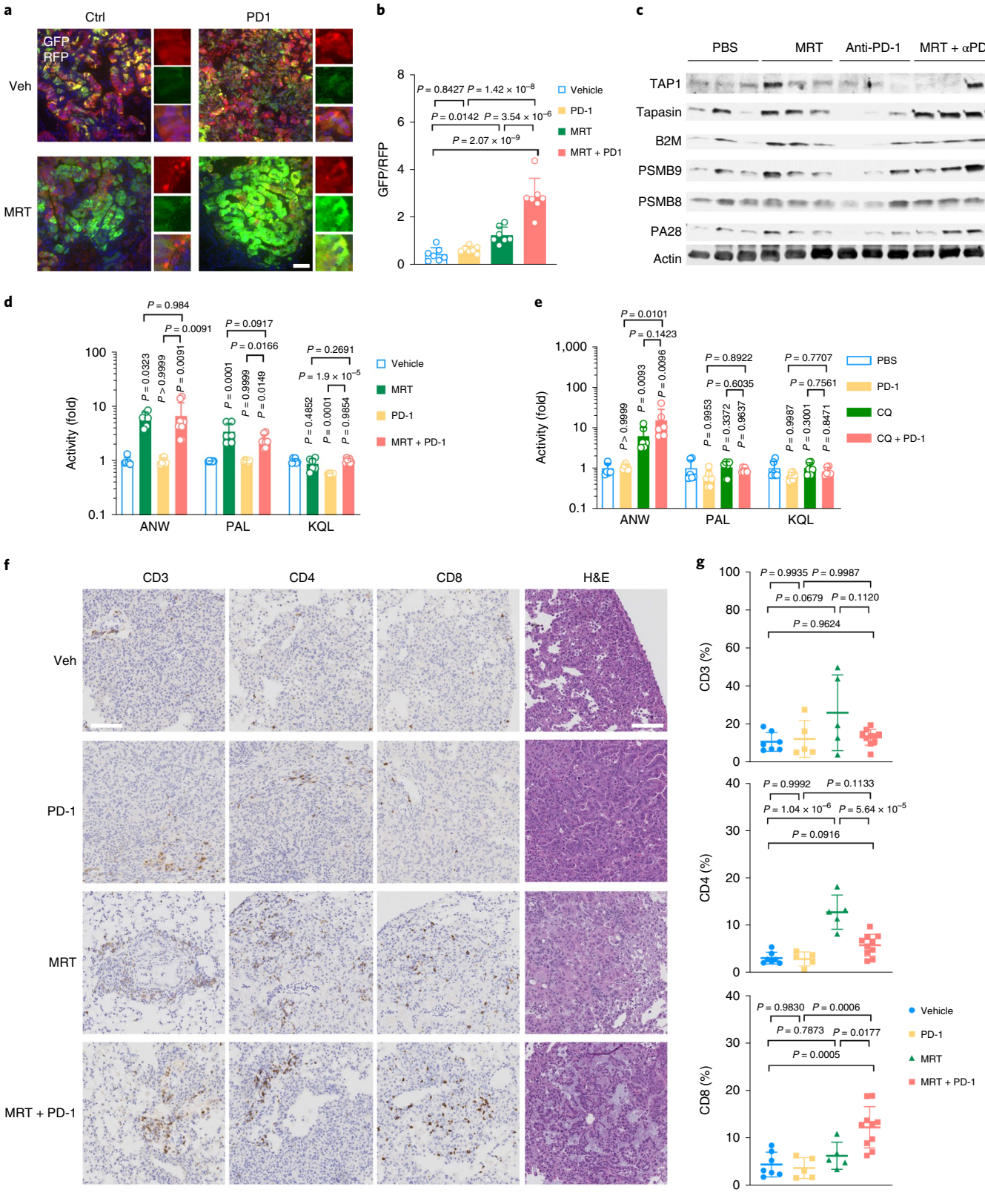

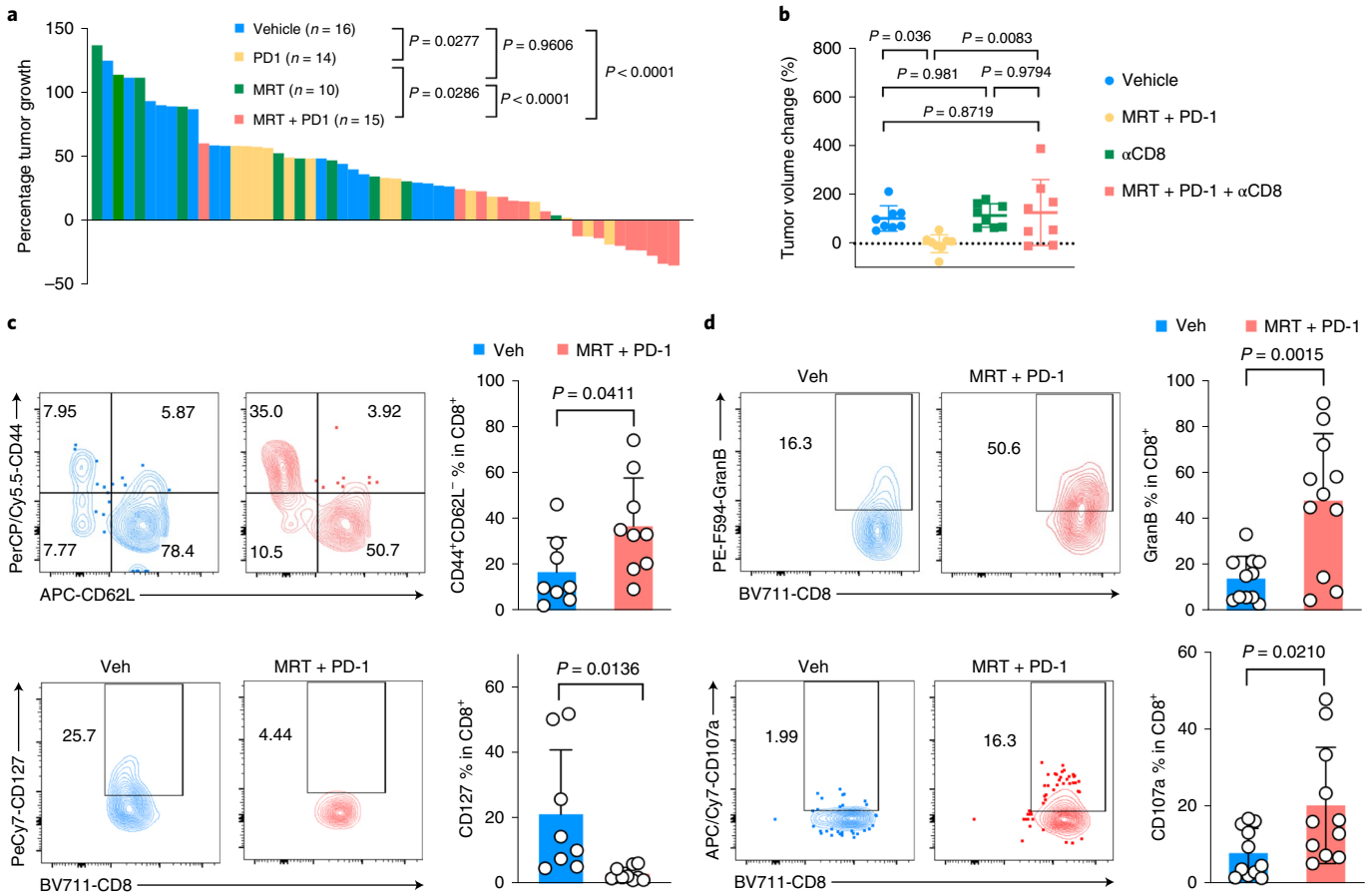

Fig. 6 | ULK1 inhibition restores antitumor immunity in *LKB1*-mutant lung cancers. a, Waterfall plot showing KL GEMM tumor volume changes 1 week after the drug treatment as indicated. Shown are the tumor volume percentage changes compared with week 0 tumor volume before the treatment. Each column represents one mouse (one-way ANOVA, Dunnett's multiple comparisons test, two-sided). **b**, Tumor volume change of KL allograft tumor 1 week after CD8$^+$ neutralizing antibody with or without MRT68921 + PD-1 combinational treatment. $n = 8$ independent mice each group (mean ± s.d., one-way ANOVA, Dunnett's multiple comparisons test, two-sided). **c**, FACS analysis of CD44$^+$ CD62L$^-$ (upper panel) and CD127$^+$ (lower panel) cells among total tumor infiltrating CD8$^+$ T cells in KL tumor after the treatment of drugs indicated. Contour plots representative of three independent experiments. Veh $n = 8$, MRT + PD-1 $n = 9$ independent tumors (mean ± s.d., two-tailed *t*-test, unpaired). **d**, Granzyme B (GranB) and CD107a levels within CD8$^+$ T cells after MRT68921 + PD-1 treatment. Left panels, representative flow panels; right panels, quantification of GranB and CD107a levels in CD8$^+$ T cells. Contour plots representative of three independent experiments. Veh $n = 11$, MRT + PD-1 $n = 11$ independent tumors (mean ± s.d., two-tailed *t*-test, unpaired).

high TMB and an increased number of neoantigens, patients with *LKB1* mutations respond poorly to anti-PD-1 treatment. Our preclinical evidence indicates that LKB1 loss leads to restricted antigen presentation to MHC complexes due to increased autophagic flux and suppressed proteasomal degradation of antigenic peptides. Further studies will be needed to determine whether the DNA repair defects and reduced antigen presentation are functionally related or represent separate functions of LKB1. In this regard, LKB1 is the upstream kinase activating the 14 members of the AMPK-SIK-MARK family, which connect LKB1 to pleiotropic functions, including regulation of cell metabolism and cell polarity[42]. These functions generally favor restoration of cellular homeostasis in response to changes in nutrient cues and oppose growth. Overall, the integration of these activities, as well as DNA repair and immune regulation reported in the present study, is in keeping with the evolutionarily conserved roles of LKB1 in mediating nutrient stress responses. Inhibiting autophagy by targeting ULK1 or downstream key regulators restores suppression of antigen presentation through enhancing immunoproteasome activity, leading to increased T cell infiltration and enhanced response to anti-PD-1 treatment through the expansion of CD44$^+$ CD62L$^-$ effector CD8$^+$ T cells in *LKB1*-mutant tumors. Potential dual effects of ULK inhibitors on both cancer cells and immune populations remain to be explored. Our findings provide the preclinical rationale for combining autophagy inhibition to enhance tumor neoantigen presentation and anti-PD-1 therapy in high-TMB tumors with inactivating mutations in *LKB1*.

Methods

RNA-sequencing and whole-exome sequencing (WES). For KP and KL cell lines and GEMMs lung nodules, RNA was extracted using RNeasy Plus Mini Kit (Qiagen). RNA-sequencing (RNA-seq) libraries were prepared using the Illumina TruSeq Stranded mRNA Library Prep (for 96 samples, catalog no. 20020595), starting from 500 ng of total RNA, with ten cycles of PCR amplification. Total genomic DNA were extracted using DNeasy Blood & Tissue Kit (Qiagen) according to the manufacturer's manual. Mouse exome libraries were prepared using Roche SeqCap EZ mouse exome kit (54 Mb, catalog no. L2RD02), starting with 250 ng of genomic DNA, following the manufacturer's protocol (Nimblegen SeqCap EZ Library SR, v.5.1). All libraries (exomes and RNA-seq) were uniquely barcoded with IDT 8 bp indices, pooled and sequenced on a NovaSeq 6000, on an S4 300 flow cell, as paired-end 150 reads or an Illumina HiSeq2500, producing 2 × 50 bp paired-end reads with multiplexing.

Whole-exome sequencing and RNA-seq small nucleotide variants analysis. Sequencing results were demultiplexed and converted to FASTQ format using Illumina bcl2fastq software (v.2.17). The reads were adapter and quality trimmed with Trimmomatic (v.0.33)[43].

For whole-exome samples, the sequencing reads were aligned to the mouse reference genome (build mm10/GRCm38) using the Burrows–Wheeler Aligner (v.0.7.17) with the BWA-MEM algorithm[44]. Low confidence mappings (mapping quality <10) and duplicate reads were removed using Sambamba[45]. Further local indel realignment and base-quality score recalibration was performed using the Genome Analysis Toolkit (GATK v.3.8)[46].

For RNA-seq samples, the sequencing reads were aligned to the mouse genome (build mm10/GRCm38) using the splice-aware STAR aligner (v.2.5.3)[47] discarding multi-mapped reads and MAPQ set to 60 for uniquely mapping reads. Duplicate reads were removed using Sambamba (v.0.6.7). GATK was used to split reads into exon segments and hard-clip any sequences overhanging into the intronic regions, followed by local indel realignment and base-quality score recalibration.

Single-nucleotide and small indel somatic variants were called with Mutect (v.2.1)[48] and Strelka (v.2.9.2)[49]. Variants with at least five supporting reads and variant allele frequencies of >5% were retained. ANNOVAR[50] was used to annotate variants with genomic context such as functional consequence on genes. The MutationalPatterns (v.1.4.3)[51] R package was used to quantify the contribution of COSMIC mutational signatures.

Patients' mutational burden analysis. *STK11* somatic mutation status, TMB and smoking history were obtained for 1,497 patients with lung cancer from the Memorial Sloan Kettering Cancer Center clinical sequencing cohort on 10 December 2018 as previously reported[13]. The $\log_{10}$-transformed TMB values were compared between *STK11*-mutant and *STK11*-wildtype tumors separately for either those who had never smoked or current and former heavy smokers using an unpaired nonparametric Mann–Whitney test (two-tailed). Shapiro–Wilk normality test was performed to determine the normal distribution of each group (confidence level 95%).

Patients' transcriptomic data and comparison groups. Lung adenocarcinoma mutation and transcriptomic data were procured from the publicly available Cancer Genome Atlas (TCGA) database[8]. From these data, we extracted all the samples that had a TP53 mutation and from this cohort we derived two groups: (1) a group with only *TP53* mutations that we designated KP ($n=22$) and (2) a group with cooccurring *STK11*/*LKB1* mutation that we designated KL ($n=19$). Silent mutations were not used for this grouping; the *STK11* mutations fell into broad missense, nonsense, splice-site and frame shift deletion variant classifications.

RNA-seq pathway analysis and GSEA. For the KL and KP cell-line and mouse nodule RNA-seq data, fastq files were aligned to the mouse mm10 reference genome using the STAR aligner algorithm[47]. Resulting BAM files were sorted and indexed using Samtools and quality control was performed using Picard (http://broadinstitute.github.io/picard/). Transcript read counts were determined was performed using Salmon[52]. Genes with no reads across any of the samples were removed. Salmon gene-level counts upper quartile normalized[53]. Genes were $\log_2$ transformed and filtered for 80% of expressed genes across all samples using Cluster v.3.0 and zeros were preserved for signature analysis. Data were then median centered to establish the matrix in working form for statistical analyses.

We used GSEA (v.3.0)[54] through the GenePattern platform[55] with publicly a available raw transcriptomic data matrix[8]. The data matrix was upper quartile normalized, log transformed, filtered for 80% of expressed genes and median centered such as the cell-line and mouse nodule data.

Besides GSEA, we performed differential gene expression analysis using the DESeq2 R package[56]. Also, using identified genes that are upregulated and downregulated, we interrogated and report their relevance in gene ontologies and pathways using the ToppGene Suite[57]. For the enrichment results, we performed 1,000 permutations using the curated set 5 gene ontology list (c5.all.v6.2.symbols.gmt.), the curated set 2 KEGG and REACTOME pathway lists (c2.cp.kegg.v6.2.symbols.gmt., c2.cp.reactome.v6.2.symbols.gmt.) and the hallmark list (h.all.v6.2.symbols.gmt.).

Cell lines. For KL and KP Ulk1 shRNA stable cell-line generation, lentiviral vector for Ulk1 shRNA (Sigma TRCN0000319764 and TRCN0000028768) or control pLKO.1 vector (Sigma catalog no. SHC001) was used. For the lentivirus production, human embryonic kidney 293T (HEK293T) cells were cotransfected with the three-vector system including pLKO.1-shRNA vector and packaging vectors psPAX2 (Addgene catalog no. 12260) and pMD2.G (Addgene catalog no. 12259). Before infection, cell culture supernatant was passed through a 0.45-µm syringe filter (Corning catalog no. 431220) and the filtered virus was added to KL cells in the presence of polybrene (10 µg ml^{-1}, Sigma catalog no. TR-1003-G) and selected with Puromycin (Sigma catalog no. P9620) 48 h after infection. Selected stable cell lines were validated by western blot and maintained in the cell culture media with 2 µg ml^{-1} puromycin.

Generation of isogenic lines with an empty vector (pBABE) (Addgene no. 1764), wildtype LKB1 (pBABE-LKB1, Addgene catalog no. 8592) and LKB1-KD (Addgene catalog no. 8593) were performed similarly to those previously described[58]. Briefly, HEK293T cells were transfected with the pBABE-LKB1, LKB1-KD or pBABE vectors, along with pCL-Eco (Addgene Plasmid catalog no. 12371) and pCMV-VSV-G (Addgene catalog no. 8454) packaging vectors.

For Atg knockdown cell-line generation, shRNA vectors were obtained from Sigma MISSION TRC shRNA library with clone ID as follows: shAtg7#1 (mouse) TRCN0000305991, shAtg7#2(mouse) RCN0000375444, shAtg13#1 (mouse) TRCN0000277121, shAtg13#2 (mouse) TRCN0000176029, shGFP TRCN0000072186. GFP–LC3–RFP (Addgene, plasmid 117413), pINDUCER20-mStrawberry and pINDUCER20-mStrawberry-Atg4BC74A were gifts from A. Kimmelman[59]. KL GFP shRNA, Atg7 shRNA, Atg13 shRNA, GFP-LC3-RFP and Atg4BC74A stable cell lines were generated using the lentiviral packaging system described above.

DNA repair assays. To measure the repair of an I-SceI generated DSB by transient transfection, for either HR or NHEJ, the assay was performed as previously reported with modifications[60]. Indicated cells were transfected with 1 µg ml^{-1} pRRL.SceI.BFP vector (Addgene catalog no. 32628) along with either 1 µg ml^{-1} pDRGFP (Addgene catalog no. 26475) for HR measurement or with 1 µg ml^{-1} of pimEJ5GFP plasmid (Addgene catalog no. 44026) for NHEJ measurement. Cells were collected 3 d after transfection, stained with zombie near infrared (NIR) fixable viability kit (Biolegend) and fixed with fixation/permeabilization solution (BD Biosciences) before fluorescence-activated cell sorting (FACS) analysis on BD LSRfortessa X-20 flow cytometer (BD Biosciences). Blue fluorescent protein (BFP) positive zombie NIR$^-$ viable cells were gated for SceI$^+$ cells. Within these BFP$^+$ NIR$^-$ cells, GFP$^+$ cell percentage was quantified using FlowJo software (BD v.10.6.1). Each condition was done at least three times and repeated for three independent experiments.

Immunofluorescence microscopy. Cells were permeabilized with cold CSK buffer (10 mM HEPES pH 7.4, 100 mM NaCl, 300 mM sucrose, 3 mM $MgCl_2$, 1 mm EGTA) containing 0.5% Triton X-100, washed with PBS, and fixed with 4% paraformaldehyde (Electron Microscopy Sciences) before blocking. Cells were blocked with 3% BSA in PBS before incubation with the indicated primary antibodies. Alexa Fluor 555 or Alexa Fluor 488-conjugated secondary antibodies (Life Technology Corporation) were added for 1 h (1:2,000 dilution). Slides were mounted in ProlongGold with 4,6-diamidino-2-phenylindole (Invitrogen). Imaging was performed using a DeltaVision Elite inverted microscope system (Applied Precision), using a ×100/1.4 numerical aperture (NA) Oil PSF Objective from Olympus. The system was equipped with a CoolSNAP HQ2 camera and SoftWorx imaging software v.5.0. Serial optical sections obtained 0.2 µm apart along the *z* axis were processed using the SoftWorx deconvolution algorithm and projected into one picture using SoftWorx software (Applied Precision).

Immunoprecipitation and immunoblotting. HEK293T cells were transiently transfected using polyethylenimine. Where indicated, 48 h after transfection, HEK293T cells were incubated with NCS for 3 h before collection. Cell lysis was carried out with lysis buffer (50 mM Tris pH 8.0, 250 mM NaCl, 10% glycerol, 1 mM EDTA, 50 mM NaF and 0.5% NP-40) supplemented with protease and phosphatase inhibitors. Where indicated, Benzonase (Sigma-Aldrich) was used at 1 U µl^{-1}. Lysates were then immunoprecipitated with anti-FLAG antibody conjugated to agarose. For chromatin fractionation cells were lysed followed by immunoblotting.

Immunoblotting. Each sample was solubilized with lysis buffer (50 mM Tris pH 7.4, 150 mM NaCl, 1 mM EDTA, 10% glycerol, 0.1% NP-40, protease inhibitors and phosphatase inhibitors). Cell extracts were quantified with primary antibodies used as LC3B (Novus Biologicals catalog no. NB100-2220), p63 (MBL catalog no. PM045), LKB1 (Cell Signaling catalog no. 3047) and β-actin (Sigma catalog no. A5441), RAD51 (GeneTex catalog no. GTX70230), pH2AX (Cell Signaling catalog no. 9718S), Histone H3 (Abcam catalog no. ab1791), PARP1 (Cell Signaling catalog no. 9542S), TAP1 (Cell Signaling catalog no. 12341S), Tapasin (Biolegend catalog no. 696702), B2M (R&D Systems MAB8325), PSMB9/LMP2 (Abcam catalog no. ab3328), PSMB8/LMP7 (Cell Signaling catalog no. 13635S), PA28 (Cell Signaling catalog no. 2409S), PSMB5 (Cell Signaling catalog no. 12919S), PSMB6 (Cell Signaling catalog no. 13267S), Atg7 (Cell Signaling catalog no. 8558S), Atg13 (Cell Signaling catalog no. 13273S), pTBK1 (Cell Signaling 5483S), TBK1 (Cell Signaling 3504S) and STING (Cell Signaling 13647S). Secondary antibodies were either coupled with horseradish peroxidase (Amersham-GE) and visualized by enhanced chemiluminescence substrate (ThermoFisher Scientific) and the signal was acquired using ImageQuant LAS 400 (GE), or the secondary antibodies of IRDye 680RD goat antirat (Li-COR catalog no. 926-68076), golden Syrian and Armenian hamster IgG DyLight 800 (Rockland catalog no. 620-145-440), IRDye 680RD donkey antimouse IgG (Li-COR catalog no. 925-68072) and IRDye 800CW donkey antirabbit IgG (Li-COR catalog no. 925-32212) were used and the fluorescent signals on the membrane were imaged on a Odyssey classic infrared imaging system (Li-COR) using Image Studio Lite (v.5.2). The results were further analyzed using ImageJ Fuji (v.1.51s).

Real-time quantitative PCR. Cell-line mRNA was isolated using the RNAeasy Mini Kit (Qiagen), quantified and 2 µg of complementary DNA per sample was synthesized using the iScript cDNA Synthesis Kit (Bio-Rad). Quantitative PCR analysis was conducted using 20 ng of cDNA per well in technical triplicates with the PowerUp SYBR Green Master Mix (ThermoFisher) and analyzed on

the Applied Biosystems StepOne Real-Time PCR using ΔΔ*Ct* quantification (ThermoFisher). Primers for each gene are listed in Supplementary Table 2.

Cell lysate immunoproteasome activity assay. Cells from individual cell lines were plated overnight, and stimulated with IFNγ at the indicated concentrations for 24 h. The immunoproteasome activities of these cells were performed using the Immunoproteasome Activity Fluorometric Assay Kit (UBPBio catalog no. J4170) according to the manual. Briefly, the lysates were generated by washing cells with cold PBS and lysing the result cell pellets, and lysates were obtained using ice cold cell lysis buffer according to the manufacturer's manual. Total cell lysate proteins (5 µg) were diluted in 1× assay buffer. Activity assay was carried out over 1 h following twofold sample dilution with 100 µM Ac-ANW-AMC, Ac-KQL-AMC or Ac-PAL-AMC substrate at 37 °C. Activity measurements were performed on a FlexStation 3 multi-mode microplate reader at wavelengths of excitation $\lambda = 360$ nm and emission $\lambda = 460$ nm with reading intervals of 1 min using Softmax Pro software (v.5.4.6.005). Each treatment condition was done in triplicate. Michaelis–Menten calculations were performed using a nonlinear fit in Prism v.8.2.0 to determine V_{max}.

TEM. Cultured cells were treated with EBSS for 1 h before being fixed in 0.1 M sodium cacodylate buffer (pH 7.2) containing 2.5% glutaraldehyde and 2% paraformaldehyde for 2 h, and then post fixed with 1% osmium tetroxide and 1% potassium ferrocyanide for 1 h at 4 °C; later they were block stained in 0.25% aqueous uranyl acetate, processed in a standard manner and embedded in EMbed 812 (Electron Microscopy Sciences). Ultrathin sections (60 nm) were cut, mounted on copper grids and stained with uranyl acetate and lead citrate. Stained grids were examined under a Philips CM-12 electron microscope and photographed with a Gatan (4,000 × 2,700) digital camera.

Autophagy analysis. For investigation of autophagy flux, a tandem autophagy flux reporter plasmid comprising mCherry-EGFP-LC3B (Addgene catalog no. 22418, a gift from J. Debnath) was used to generate the indicated cells that were treated with MRT followed by imaging of the LC3 puncta using a Leica DM6, and image acquisition was done using LAS X software (v.2.0.0.14332.2). For quantification of autophagic flux, tandem GFP-RFP-LC3 reporter construct ptfLC3 plasmid (Addgene catalog no. 21074) was transfected into indicated cells. Cells were treated with either vehicle control or MRT68921 (MCE, catalog no. HY-100006A) for 24 h, followed by EBSS nutrient deprivation for 3 h, and collected for quantification of autophagic flux as determined by the fluorescent signal of the red fluorescent protein (RFP) to GFP ratio within live cells. Data were acquired by FACS using LSRFortessa X-20 (BD) and analyzed using FlowJo software (BD v.10.6.1).

For autophagy flux analysis using western blot, each group of cells was treated with Bafilomycin A1 (Cayman Chemical Company, catalog. no. 11038) and/or MRT68921 with EBSS (ThermoFisher Scientific, catalog no. 24010043) for 1 h. Cells were collected and protein extractions were quantified for immunoblotting with the indicated antibodies. For autophagy flux analysis in vivo, tumors with GFP-LC3-RFP reporter were collected after indicated drug treatment and quantified by ratio of RFP to GFP using immunofluorescence staining or FACS analysis.

Animal studies. All animal studies were reviewed and approved by the Institutional Animal Care and Use Committee (IACUC) at the New York University School of Medicine. The GEMM harboring a conditional activating mutation of endogenous Kras (*Kras*$^{LSL\text{-}G12D/+}$) crossed with *Lkb1* or *p53* conditional knockout (*Lkb1*$^{fl/fl}$ or *Trp53*$^{fl/fl}$) has been previously described[13]. All the mice were crossed and confirmed with C57BL/6 genetic background by single-nucleotide polymorphism analysis, 99.59% for KP (*Kras*^{G12D}*Trp53*$^{fl/fl}$), 94.46% for KL (*Kras*^{G12D}*Lkb1*$^{fl/fl}$). CRE recombinase was induced through intranasal inhalation of 1×10^7 plaque forming units of adeno-Cre (University of Iowa adenoviral core). The induced mice were evaluated by MRI imaging to quantify the lung tumor burden, and KP and KL lung tumor nodules were obtained and tumor cell lines were generated from these nodules ex vivo. Briefly, lung tumors were harvested and washed twice in 1× PBS, and then the tumors were cut into small pieces using scissors. The shredded tissues were cultured in an incubator at 37 °C (with 5% CO_2). Fresh medium was changed every other day. The cells were cultured for at least five passages to establish the stable cell lines. In this study, five KL cell lines generated from different KL mice were used. Generated KL cells were injected into female B6(Cg)-*Tyr*$^{c\text{-}2J}$/J (B6-albino) mice via tail vein injection at 1×10^6 per mice. Both KL GEMMs and KL allografts and lung tumor developments were examined via MRI scan by a 7-T Bruker Biospec 70/30 MRI System and the images were acquired using ParaVision software (v.6). Mice lung tumor burdens were quantified by MRI imaging before and after the drug treatment. MRT68921 (MedChemExpress, catalog no. HY-100006A) or PBS vehicle control was administered as 15 mg kg^{-1} through intraperitoneal (i.p.) injection daily; PD-1 antibody PD-1 (clone 29F.1A12) was administered three times a week at 200 µg per mouse through i.p. injection. Chloroquine diphosphate (Sigma, catalog no. C6628-25G) was administered as 60 mg kg^{-1} through i.p. injection daily alone or in combination with anti-PD-1 antibody. For CD8 depletion assay, anti-CD8 (clone 2.43, Bioxcell, catalog no. BP0061) antibodies were injected at 400 µg per mouse via i.p. injection twice a week 3 d before the MRT68921 + PD-1 antibody treatment began.

Cell isolation for immune analysis. Mouse lungs with tumors were collected after being transcardially perfused with ice cold 1× PBS, followed by mechanical disruption with scissors. The minced tissues were incubated with lysis buffer of Hank's balanced salt solution (ThermoFisher Scientific catalog no. 14025092) with collagenase D (400 U ml^{-1}, Sigma catalog no. 11088866001) and DNase I (1 mg ml^{-1}, Sigma catalog no. 10104159001) at 37 °C for 30 min. The digested tissue was separated through a 70-µm cell strainer to obtain a single cell suspension. Cells were spun down at 1,500 r.p.m. for 5 min at 4 °C (Eppendorf centrifuge 5810R). Pellets were lysed with 1× RBC lysis buffer (Biolegend catalog no. 420301) and cells were further processed for downstream applications.

Antibodies for flow cytometric analysis. For mouse studies, the following antibodies were purchased from Biolegend: CD45 (clone 30-F11), CD4 (clone RM4-5), CD8 (clone 53-6.7), CD3 (clone 17A2), PD-1 (clone 29F.1A12), CD69 (clone H1.2F3), CCR7 (clone 4B12), CD244/2B4 (clone m2B4), CD44 (clone IM7), CD62L (clone MEL-14), CD127 (clone A7R34), CD107a (clone 1D4B) and MHCI (clone M1/42). From BD Biosciences, Granzyme B (GB1). From eBiosciences, Foxp3 (clone FJK-16s) and CTLA-4 (clone UC10-4B9). Cells were stained and analyzed using BD Fortessa with DACS Diva (v.8.0.1) and FlowJo software (v.10.6.1).

Cell growth assay. Adherent syngeneic KL and KP cells were plated in 96-well plates at a density of 1,000 cells per well overnight and challenged with 1 nM–20 µM of each compound as indicated for 72 h in the presence of 10% FBS and constant 0.2% dimethylsulfoxide (DMSO) in RMPI-1640. Cell proliferation was measured by CCK-8 kit (Enzo Lifesciences, catalog no. ALX-850-039-KI02) as per the manufacturer's protocol on a FlexStation 3 multi-mode microplate reader using Softmax Pro software (v.5.4.6.005). The data calculations were carried out as the percentage cell growth over the DMSO controls and half-maximum inhibitory concentration (IC_{50}) was acquired using CalcuSyn (v.2). The normalized data were then $\log_{10}$ transformed and plotted in GraphPad Prism v.8.

Statistics and reproducibility. No statistical methods were used to predetermine sample size. The group size of mice and samples were chosen based on our previous publications that we used to generate statistically significant results[58]. The experiments for the animal study were not randomized and the investigators were not blinded during the experiment and outcome assessment. Randomization is not relevant to other cell-based studies since they require different treatment conditions. For immunofluorescence microscopy, one sample (KL + LKB1) was excluded during foci quantification due to cell contamination (Fig. 2f). For comparison of normal distribution samples, a two-tailed *t*-test was used for statistical analysis using Prism software. For multiple comparisons, a one-way analysis of variance (ANOVA) or multiple *t*-test was used as specified for each experiment in the figure legend with *P* values calculated in Prism. For patient samples that are not in a normal distribution, the Shapiro–Wilk test was used for a normality test and a Mannn–Whitney test was used for statistical analysis among different groups.

Reporting Summary. Further information on research design is available in the Nature Research Reporting Summary linked to this article.

Data availability

All data generated and supporting the findings of this study are available within the paper. The RNA-seq data have been deposited in the Gene Expression Ominbus accession number GSE137244 and GSE137396. The whole-exome sequencing data have been deposited in the NCBI Sequence Read Archive accession number PRJNA564395. TCGA data used are publicly available at the Genomic Data Commons portal (https://portal.gdc.cancer.gov/). Source data are available for this paper. All other data supporting the findings of this study are available from the corresponding author on reasonable request.

Received: 17 November 2020; Accepted: 9 April 2021;
Published online: 17 May 2021

References

1. Skoulidis, F. et al. STK11/LKB1 mutations and PD-1 inhibitor resistance in KRAS-mutant lung adenocarcinoma. *Cancer Discov.* **8**, 822–835 (2018).
2. Kadara, H. et al. Whole-exome sequencing and immune profiling of early-stage lung adenocarcinoma with fully annotated clinical follow-up. *Ann. Oncol.* **28**, 75–82 (2017).
3. Rizvi, H. et al. Molecular determinants of response to anti-programmed cell death (PD)-1 and anti-programmed death-ligand 1 (PD-L1) blockade in patients with non-small-cell lung cancer profiled with targeted next-generation sequencing. *J. Clin. Oncol.* **36**, 633–641 (2018).
4. Herter-Sprie, G. S. et al. Synergy of radiotherapy and PD-1 blockade in Kras-mutant lung cancer. *JCI Insight* **1**, e87415 (2016).

5. Xu, C. et al. Loss of Lkb1 and Pten leads to lung squamous cell carcinoma with elevated PD-L1 expression. *Cancer Cell* **25**, 590–604 (2014).
6. Koyama, S. et al. STK11/LKB1 deficiency promotes neutrophil recruitment and proinflammatory cytokine production to suppress T-cell activity in the lung tumor microenvironment. *Cancer Res.* **76**, 999–1008 (2016).
7. Deng, J. et al. CDK4/6 inhibition augments antitumor immunity by enhancing T-cell activation. *Cancer Discov.* **8**, 216–233 (2018).
8. Cancer Genome Atlas Research, N. Comprehensive molecular profiling of lung adenocarcinoma. *Nature* **511**, 543–550 (2014).
9. Rizvi, N. A. et al. Cancer immunology. Mutational landscape determines sensitivity to PD-1 blockade in non-small cell lung cancer. *Science* **348**, 124–128 (2015).
10. McGranahan, N. et al. Clonal neoantigens elicit T cell immunoreactivity and sensitivity to immune checkpoint blockade. *Science* **351**, 1463–1469 (2016).
11. Schumacher, T. N. & Schreiber, R. D. Neoantigens in cancer immunotherapy. *Science* **348**, 69–74 (2015).
12. McFadden, D. G. et al. Mutational landscape of EGFR-, MYC-, and Kras-driven genetically engineered mouse models of lung adenocarcinoma. *Proc. Natl Acad. Sci. USA* **113**, E6409–E6417 (2016).
13. Cheng, D. T. et al. Memorial Sloan Kettering-integrated mutation profiling of actionable cancer targets (MSK-IMPACT): a hybridization capture-based next-generation sequencing clinical assay for solid tumor molecular oncology. *J. Mol. Diagn.* **17**, 251–264 (2015).
14. Govindan, R. et al. Genomic landscape of non-small cell lung cancer in smokers and never-smokers. *Cell* **150**, 1121–1134 (2012).
15. Turajlic, S. et al. Insertion-and-deletion-derived tumour-specific neoantigens and the immunogenic phenotype: a pan-cancer analysis. *Lancet Oncol.* **18**, 1009–1021 (2017).
16. Mandal, R. et al. Genetic diversity of tumors with mismatch repair deficiency influences anti-PD-1 immunotherapy response. *Science* **364**, 485–491 (2019).
17. Alexandrov, L. B. et al. Signatures of mutational processes in human cancer. *Nature* **500**, 415–421 (2013).
18. Davies, H. et al. HRDetect is a predictor of BRCA1 and BRCA2 deficiency based on mutational signatures. *Nat. Med.* **23**, 517–525 (2017).
19. Helleday, T., Eshtad, S. & Nik-Zainal, S. Mechanisms underlying mutational signatures in human cancers. *Nat. Rev. Genet.* **15**, 585–598 (2014).
20. Pierce, A. J., Johnson, R. D., Thompson, L. H. & Jasin, M. XRCC3 promotes homology-directed repair of DNA damage in mammalian cells. *Genes Dev.* **13**, 2633–2638 (1999).
21. Bennardo, N., Cheng, A., Huang, N. & Stark, J. M. Alternative-NHEJ is a mechanistically distinct pathway of mammalian chromosome break repair. *PLoS Genet.* **4**, e1000110 (2008).
22. Jasin, M. & Rothstein, R. Repair of strand breaks by homologous recombination. *Cold Spring Harb. Perspect. Biol.* **5**, a012740 (2013).
23. Panier, S. & Durocher, D. Push back to respond better: regulatory inhibition of the DNA double-strand break response. *Nat. Rev. Mol. Cell Biol.* **14**, 661–672 (2013).
24. Le, D. T. et al. PD-1 blockade in tumors with mismatch-repair deficiency. *N. Engl. J. Med.* **372**, 2509–2520 (2015).
25. Nolan, E. et al. Combined immune checkpoint blockade as a therapeutic strategy for BRCA1-mutated breast cancer. *Sci. Transl. Med.* https://doi.org/10.1126/scitranslmed.aal4922 (2017).
26. Hisamatsu, H. et al. Newly identified pair of proteasomal subunits regulated reciprocally by interferon gamma. *J. Exp. Med.* **183**, 1807–1816 (1996).
27. Boehm, U., Klamp, T., Groot, M. & Howard, J. C. Cellular responses to interferon-gamma. *Annu. Rev. Immunol.* **15**, 749–795 (1997).
28. Seliger, B. et al. IFN-gamma-mediated coordinated transcriptional regulation of the human TAP-1 and LMP-2 genes in human renal cell carcinoma. *Clin. Cancer Res.* **3**, 573–578 (1997).
29. Peaper, D. R., Wearsch, P. A. & Cresswell, P. Tapasin and ERp57 form a stable disulfide-linked dimer within the MHC class I peptide-loading complex. *EMBO J.* **24**, 3613–3623 (2005).
30. Dikic, I. Proteasomal and autophagic degradation systems. *Annu. Rev. Biochem.* **86**, 193–224 (2017).
31. Poillet-Perez, L. et al. Autophagy maintains tumour growth through circulating arginine. *Nature* **563**, 569–573 (2018).
32. Yang, A. et al. Autophagy sustains pancreatic cancer growth through both cell-autonomous and nonautonomous mechanisms. *Cancer Discov.* **8**, 276–287 (2018).
33. Bhatt, V. et al. Autophagy modulates lipid metabolism to maintain metabolic flexibility for Lkb1-deficient Kras-driven lung tumorigenesis. *Genes Dev.* **33**, 150–165 (2019).
34. Kim, H. S. et al. Systematic identification of molecular subtype-selective vulnerabilities in non-small-cell lung cancer. *Cell* **155**, 552–566 (2013).
35. Skoulidis, F. et al. Co-occurring genomic alterations define major subsets of KRAS-mutant lung adenocarcinoma with distinct biology, immune profiles, and therapeutic vulnerabilities. *Cancer Discov.* **5**, 860–877 (2015).
36. Osorio, F., Lambrecht, B. N. & Janssens, S. Antigen presentation unfolded: identifying convergence points between the UPR and antigen presentation pathways. *Curr. Opin. Immunol.* **52**, 100–107 (2018).
37. Shintani, T. & Klionsky, D. J. Autophagy in health and disease: a double-edged sword. *Science* **306**, 990–995 (2004).
38. Petherick, K. J. et al. Pharmacological inhibition of ULK1 kinase blocks mammalian target of rapamycin (mTOR)-dependent autophagy. *J. Biol. Chem.* **290**, 28726 (2015).
39. Kimura, S., Noda, T. & Yoshimori, T. Dissection of the autophagosome maturation process by a novel reporter protein, tandem fluorescent-tagged LC3. *Autophagy* **3**, 452–460 (2007).
40. Kitajima, S. et al. Suppression of STING associated with LKB1 loss in KRAS-driven lung cancer. *Cancer Discov.* **9**, 34–45 (2019).
41. Mazzucchelli, R. & Durum, S. K. Interleukin-7 receptor expression: intelligent design. *Nat. Rev. Immunol.* **7**, 144–154 (2007).
42. Shackelford, D. B. & Shaw, R. J. The LKB1-AMPK pathway: metabolism and growth control in tumour suppression. *Nat. Rev. Cancer* **9**, 563–575 (2009).
43. Bolger, A. M., Lohse, M. & Usadel, B. Trimmomatic: a flexible trimmer for Illumina sequence data. *Bioinformatics* **30**, 2114–2120 (2014).
44. Li, H. & Durbin, R. Fast and accurate short read alignment with Burrows–Wheeler transform. *Bioinformatics* **25**, 1754–1760 (2009).
45. Tarasov, A., Vilella, A. J., Cuppen, E., Nijman, I. J. & Prins, P. Sambamba: fast processing of NGS alignment formats. *Bioinformatics* **31**, 2032–2034 (2015).
46. McKenna, A. et al. The Genome Analysis Toolkit: a MapReduce framework for analyzing next-generation DNA sequencing data. *Genome Res.* **20**, 1297–1303 (2010).
47. Dobin, A. et al. STAR: ultrafast universal RNA-seq aligner. *Bioinformatics* **29**, 15–21 (2013).
48. Cibulskis, K. et al. Sensitive detection of somatic point mutations in impure and heterogeneous cancer samples. *Nat. Biotechnol.* **31**, 213–219 (2013).
49. Kim, S. et al. Strelka2: fast and accurate calling of germline and somatic variants. *Nat. Methods* **15**, 591–594 (2018).
50. Wang, K., Li, M. & Hakonarson, H. ANNOVAR: functional annotation of genetic variants from high-throughput sequencing data. *Nucleic Acids Res.* **38**, e164 (2010).
51. Blokzijl, F., Janssen, R., van Boxtel, R. & Cuppen, E. MutationalPatterns: comprehensive genome-wide analysis of mutational processes. *Genome Med.* **10**, 33 (2018).
52. Patro, R., Duggal, G., Love, M. I., Irizarry, R. A. & Kingsford, C. Salmon provides fast and bias-aware quantification of transcript expression. *Nat. Methods* **14**, 417–419 (2017).
53. Bullard, J. H., Purdom, E., Hansen, K. D. & Dudoit, S. Evaluation of statistical methods for normalization and differential expression in mRNA-seq experiments. *BMC Bioinf.* **11**, 94 (2010).
54. Subramanian, A. et al. Gene set enrichment analysis: a knowledge-based approach for interpreting genome-wide expression profiles. *Proc. Natl Acad. Sci. USA* **102**, 15545–15550 (2005).
55. Reich, M. et al. GenePattern 2.0. *Nat. Genet.* **38**, 500–501 (2006).
56. Love, M. I., Huber, W. & Anders, S. Moderated estimation of fold change and dispersion for RNA-seq data with DESeq2. *Genome Biol.* **15**, 550 (2014).
57. Chen, J., Bardes, E. E., Aronow, B. J. & Jegga, A. G. ToppGene suite for gene list enrichment analysis and candidate gene prioritization. *Nucleic Acids Res.* **37**, W305–W311 (2009).
58. Ji, H. et al. LKB1 modulates lung cancer differentiation and metastasis. *Nature* **448**, 807–810 (2007).
59. Yamamoto, K. et al. Autophagy promotes immune evasion of pancreatic cancer by degrading MHC-I. *Nature* **581**, 100–105 (2020).
60. Stark, J. M., Pierce, A. J., Oh, J., Pastink, A. & Jasin, M. Genetic steps of mammalian homologous repair with distinct mutagenic consequences. *Mol. Cell. Biol.* **24**, 9305–9316 (2004).

Acknowledgements

This work was supported by grants R01CA166480 (K.-K.W.), U01CA233084 (K.-K.W.), R01CA219670 (N.B., K.-K.W.), R01CA076584 (M.P.), SPORE P50CA058223 (C.M.P.), P50CA101942 (G.J.F.) and a fellowship from the T32 CA009161 (Levy) grant to A.M. We thank New York University (NYU) Langone Genome Technology Center for facilitating RNA-seq and whole-exome sequencing experiments. We thank the NYU Langone Division of Comparative Medicine staff for their support in the animal studies. We thank NYU Langone Health DART Microscopy Laboratory A. Liang, C. Petzold and K. Dancel-Manning for their assistance with TEM work. This core laboratory is partially funded by NYU Cancer Center Support grant no. NIH/NCI P30CA016087. M.P. is an Investigator with the Howard Hughes Medical Institute.

Author contributions

J.D. and K.-K.W. conceived and designed the experiment. J.D. did most of the experiments described in this paper. A.T. and J.D. designed and performed the pathway, gene expression and GSEA analysis. I.D. and J.D. designed and performed mutational load and mutational signature analysis. J.T.P. performed specimen TMB score analysis on

patients with NSCLC. J.D., H.S. and C.T. performed HR and microhomology-mediated end joining analysis. A.M. performed chromatin binding assay, immunoprecipitation and DSB foci analysis. M.B. and D.H.P. performed western blot for the antigen presentation pathway. M.B. and D.H.P. generated the *Ulk1* shRNA and *Atg* cell lines. F.L. and H.Hu. generated the KL cell lines. F.L., Y.P. and H.D. generated and characterized KLP cell lines. J.D., H.D., D.H.P. and H.Han performed the immunoproteasome activity assay. J.D., T.C., E.P., V.P., C.T., S.L. and H.Hu. performed animal experiments, treatment studies and MRI imaging and analysis. J.D. and E.P. performed immune analysis of the animal models. T.C. performed the cell growth assay. J.L., J.D. and S.M. performed autophagy flux analysis. J.L. performed electron microscopy experiments and analysis. J.D., B.J. and N.S.G. participated in the *Ulk1* inhibitor experiment. J.D. and N.B. drafted the paper. J.D., K.-K.W., N.B., V.W., E.S.W., P.S.H., N.S.G., T.P., A.T., M.Pagano, E.R., J.G., G.J.F., C.M.R., J.V.H., C.M.P., I.A. and M.Philips. conceptually designed and edited the paper. K.-K.W. conceived, designed and supervised all the experiments. All authors reviewed and discussed the final version of the paper.

Competing interests

The authors declare the following competing interests: K.-K.W. is a founder and equity holder of G1 Therapeutics. K.-K.W. has sponsored Research Agreements with MedImmune, Takeda, TargImmune, Mirati, Merus, Alkermes and BMS. K.-K.W. has consulting and sponsored research agreements with AstraZeneca, Janssen, Pfizer, Novartis, Merck, Ono, Array. C.M.P is an equity stock holder and consultant, and Board of Director Member of BioClassifier LLC and GeneCentric Diagnostics. C.M.P is also listed an inventor on patent applications on the Breast PAM50 and Lung Cancer Subtyping assays. C.M.R. has consulted regarding cancer drug development with AbbVie, Amgen, Ascentage, Bicycle, Celgene, Daiichi Sankyo, Genentech/Roche, Ipsen, Loxo and PharmaMar, and serves on the SAB of Bridge Medicines and Harpoon Therapeutics. M.Pagano is a cofounder of Coho Therapeutics; has financial interests in Coho Therapeutics, CullGen Inc. and Kymera Therapeutics; is on the SAB of CullGen Inc. and Kymera Therapeutics, and is a consultant for Coho Therapeutics, CullGen Inc., Kymera Therapeutics and SEED Therapeutics. J.F.G. has served as a compensated consultant or received honoraria from Bristol-Myers Squibb, Genentech, Ariad/Takeda, Loxo/Lilly, Blueprint, Oncorus, Regeneron, EMD Serono, Gilead, AstraZeneca, Pfizer, Incyte, Novartis, Merck, Agios, Amgen and Array; research support from Novartis, Genentech/Roche and Ariad/Takeda; institutional research support from Bristol-Myers Squibb, Tesaro, Moderna, Blueprint, Jounce, Array Biopharma, Merck, Adaptimmune, Novartis and Alexo; and has an immediate family member who is an employee of Ironwood Pharmaceuticals. G.J.F. has patents/pending royalties on the PD-1/PD-L1 pathway from Roche, Merck MSD, Bristol-Myers-Squibb, Merck KGA, Boehringer-Ingelheim, AstraZeneca, Dako, Leica, Mayo Clinic and Novartis. G.J.F. has served on advisory boards for Roche, Bristol-Myers-Squibb, Xios, Origimed, Triursus, iTeos, NextPoint, IgM, Jubilant and GV20. G.J.F. has equity in NextPoint, Triursus, Xios, iTeos, IgM and GV20.

Additional information

Extended data is available for this paper at https://doi.org/10.1038/s43018-021-00208-6.

Supplementary information The online version contains supplementary material available at https://doi.org/10.1038/s43018-021-00208-6.

Correspondence and requests for materials should be addressed to K.-K.W.

Peer review information *Nature Cancer* thanks Andrew Thorburn and the other, anonymous, reviewer(s) for their contribution to the peer review of this work.

Reprints and permissions information is available at www.nature.com/reprints.

Publisher's note Springer Nature remains neutral with regard to jurisdictional claims in published maps and institutional affiliations.

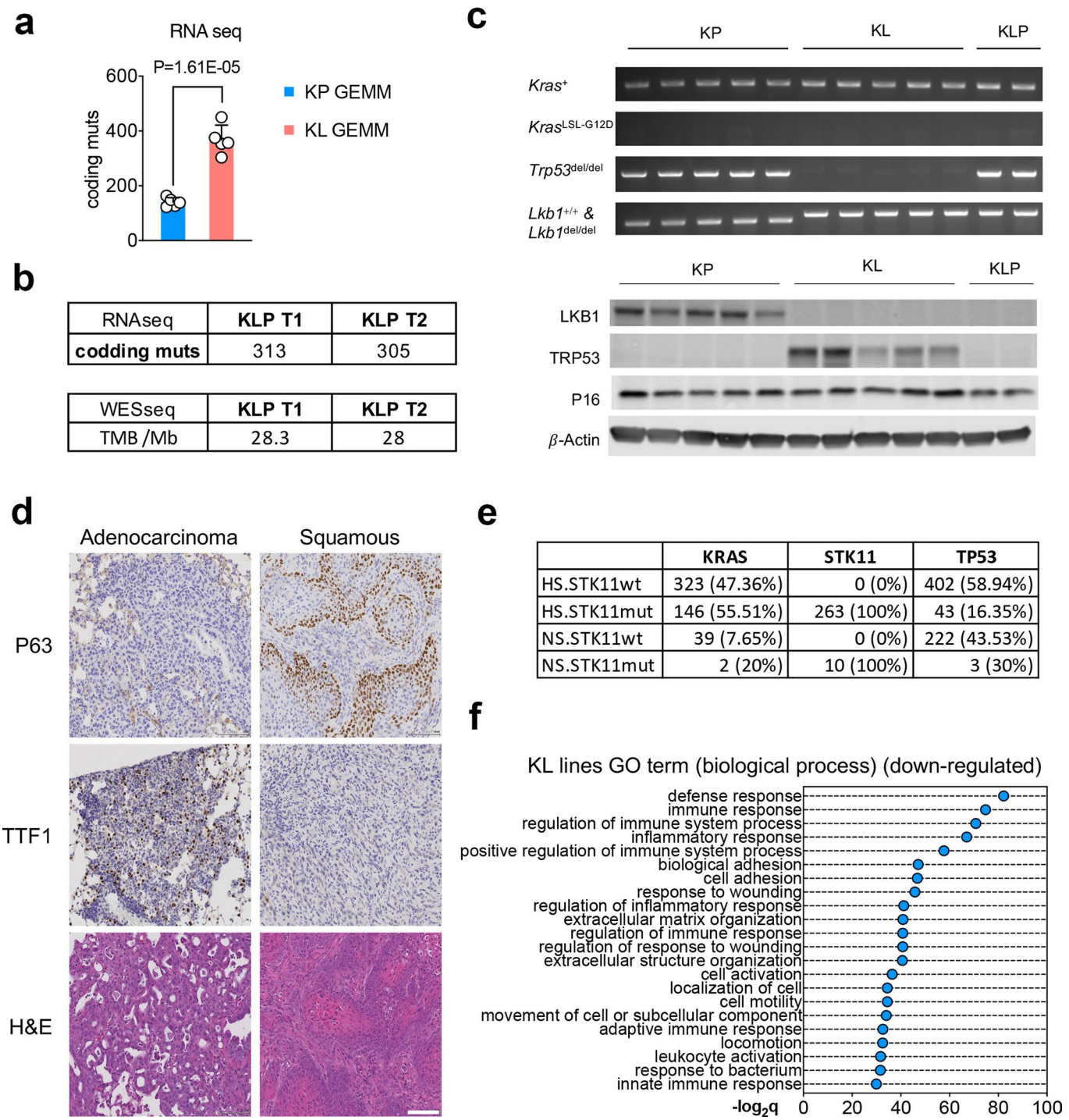

b

RNAseq	KLP T1	KLP T2
codding muts	313	305

WESseq	KLP T1	KLP T2
TMB /Mb	28.3	28

e

	KRAS	STK11	TP53
HS.STK11wt	323 (47.36%)	0 (0%)	402 (58.94%)
HS.STK11mut	146 (55.51%)	263 (100%)	43 (16.35%)
NS.STK11wt	39 (7.65%)	0 (0%)	222 (43.53%)
NS.STK11mut	2 (20%)	10 (100%)	3 (30%)

Extended Data Fig. 1 | Mutational burden and signature analysis for LKB1 mutant tumors. a, Comparison of tumor mutational burden (TMB) of nonsynonymous mutation using freshly isolate NSCLC GEMMs lung nodules from *Kras*^{G12D}*Lkb1*$^{fl/fl}$ (KL) or *Kras*^{G12D}*Trp53*$^{fl/fl}$ (KP) from RNA sequencing. n = 5 lung nod each group. (unpaired *t*-test, two sided, FDR < 0.05) **b**, TMB analysis of cell lines derived from *Kras*^{G12D}*Lkb1*$^{fl/fl}$*Trp53*$^{fl/fl}$ (KLP) NSCLC GEMM nodules using RNA sequencing (Upper table) or whole exome sequencing (WES) (lower table) for each cell line. **c**, Validation of KP, KL, KLP lines used. Upper panel, PCR result of indicated primers for each cell line. Lower panel, western blot result of LKB1, TRP53 and P16 protein levels of each cell lines. Blots are cropped and that uncropped images can be found in Source Data. Data represents one of three independent experiments. **d**, Representative IHC images of KL allograft lung tumors showing adenocarcinoma (left panels) or squamous tumor (right panels). Data represents one of three independent experiments. Scale bar, 100μm. **e**, Co-mutational analysis of NSCLC patients analyzed in Fig. 1b, including KRAS, STK11 and TP53 as total patient number and percentage within each group. **f**, Top suppressed biological process pathways from *Kras/Lkb1* comparing with *Kras/Trp53* mutant mouse cell lines. x-axis, -log$_2$q value (Bonferroni) between the two groups. n = 5 cell lines each group.

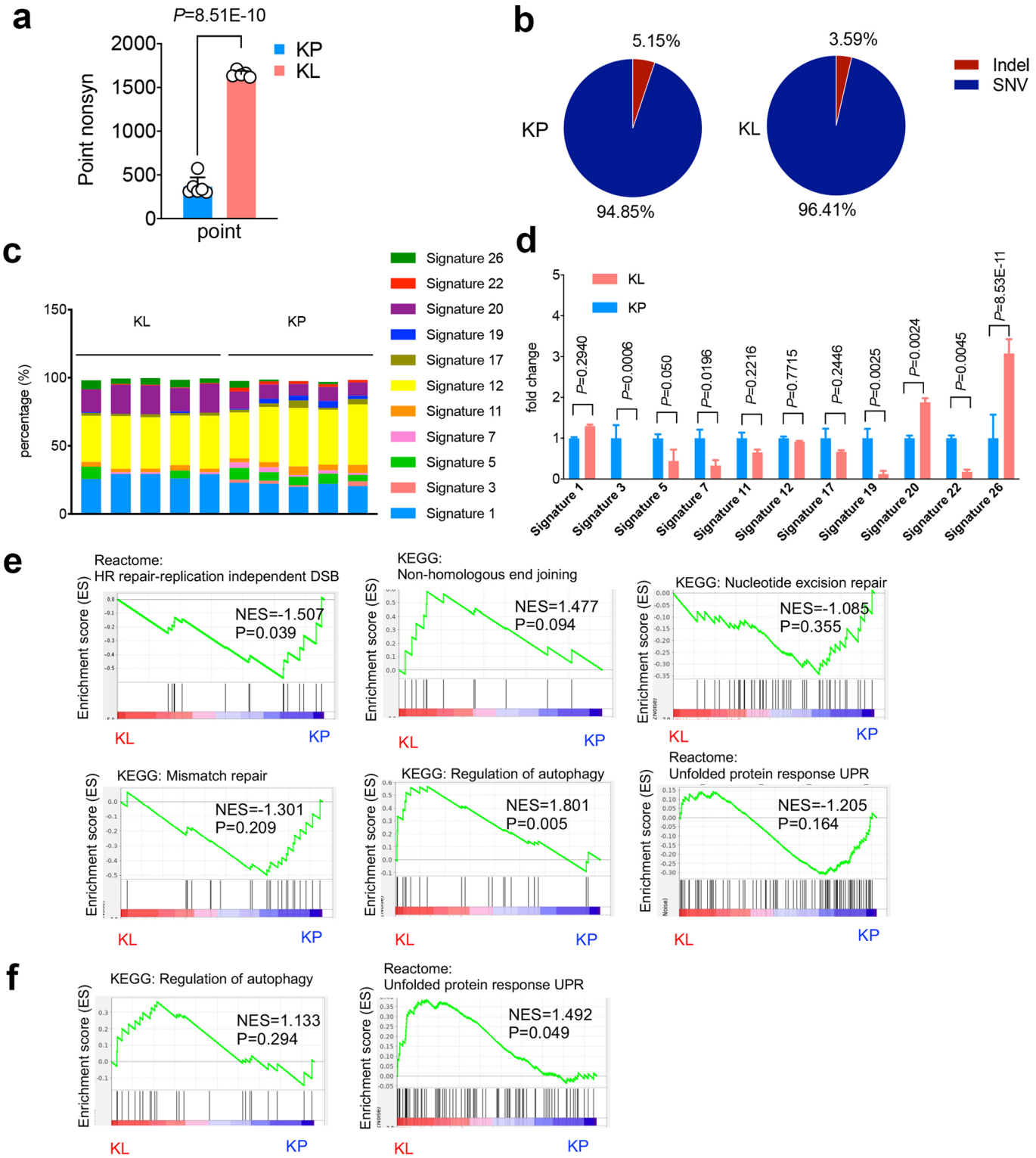

Extended Data Fig. 2 | Mutational signature analysis and gene set enrichment analysis (GSEA) from KL and KP tumors. a, Point nonsynonymous single-nucleotide variations (SNV) numbers from either KP or KL cells. KP n = 6, KL n = 5 cell lines each group. (mean±sd, unpaired *t* test, two tailed). **b**, Percentage of Indels and SNVs in KP and KL cells KP n = 6, KL n = 5 cell lines each group. (unpaired *t* test, two sided. $P = 0.0032$). **c**, Percentage of each COSMIC mutational signature detected in the cell lines examined. Each column represents one individual cell line. **d**, Fold change of the signatures shown in (a) and normalized to average levels of corresponding signature in KP. KL, KP n = 5 cell lines each group. (mean ± sd, multiple *t* test, FDR < 0.05). **e**, GSEA of DNA repair related pathways, including HR repair-replication independent DSB, non-homologous end joining, nucleotide excision repair and mismatch repair, and related autophagy pathway and unfolded protein response (UPR) pathway of KL and KP GEMM lung nodules. KL n = 5, KP n = 5 lung nodules each group. **f**, Gene set enrichment analysis (GSEA) of TCGA patients for autophagy pathway and UPR pathway. KL n = 19, KP n = 22 patients each group.

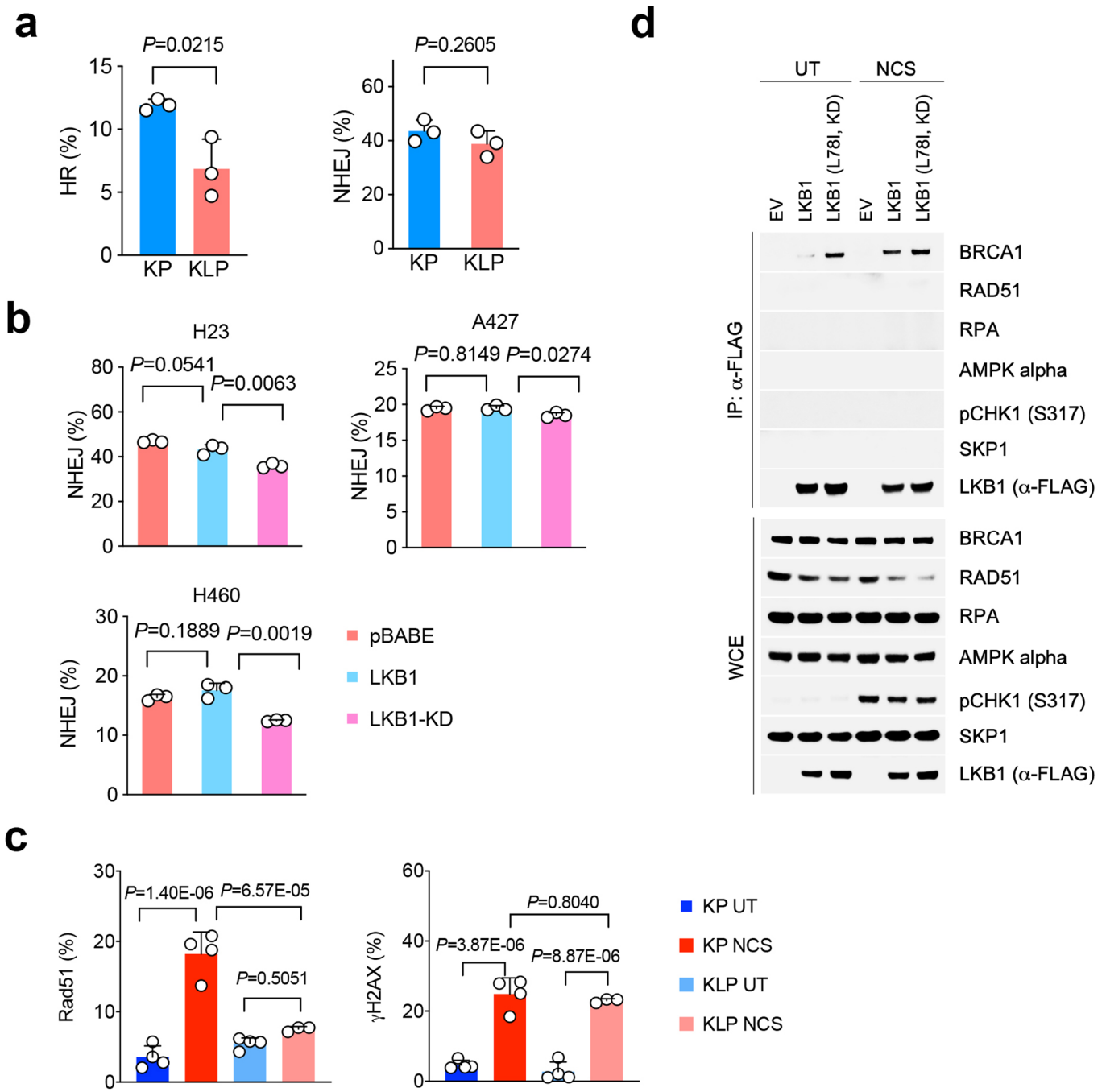

Extended Data Fig. 3 | LKB1 mutant tumor double strand break repair. a, HR and NHEJ levels in *Kras/Lkb1/Trp53* mutant cell lines comparing with Kras/Trp53 cells. n = 3 cell cultures for each group. (mean±sd, two-sided *t* test, unpaired). **b**, NHEJ ratio changes in human NSCLC LKB1 mutant cell lines H23, A427 and H460 with empty vector (pBABE), LKB1 or KLB1-KD overexpression were determined by flow cytometry. n = 3 individual cell cultures for each group. (mean±sd, two-sided *t* test, unpaired). **c**, Quantification of Rad51 and pH2AX positive cells percentage in KLP cells. Result is combined from three independent experiments. KP UT, KP NCS and KLP UT n = 4, KLP NCS n = 3 individual cell cultures each group. Data shown one of two independent experiments. (mean ± sd, one-way ANOVA, multiple two-sided comparison, Tukey test). **d**, LKB1 forms complex with BRCA1 in response to DNA damage. Upper panel, immunoprecipitation assay showing LKB1 interacting proteins in response to neocarzinostatin (NCS) treatment induced DNA damage. Lower panel, western blot showing total level of input proteins from whole-cell extract (WCE). Data represents one of two independent experiments. Blots are cropped and uncropped images can be found in Source Data.

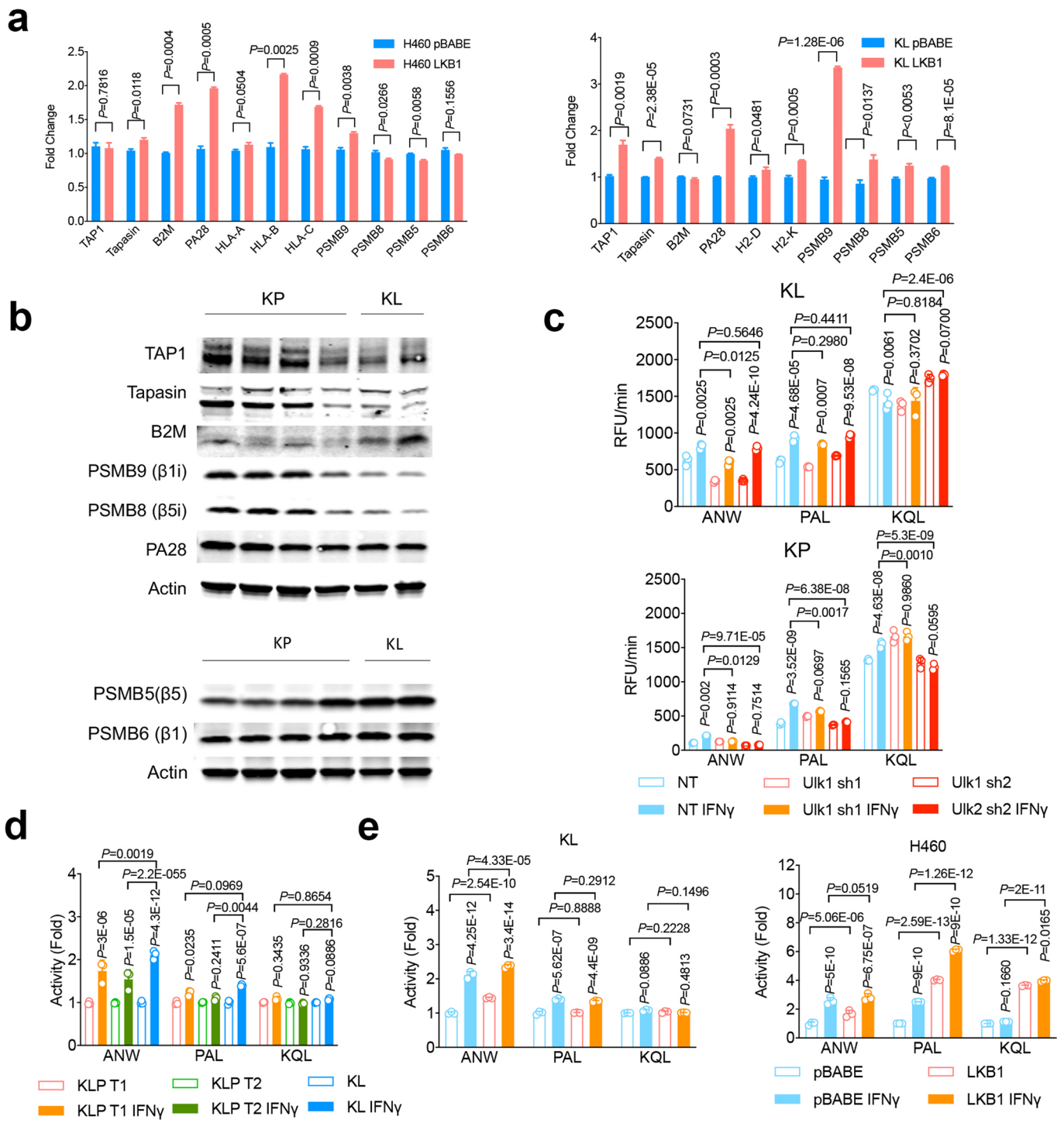

Extended Data Fig. 4 | Immunoproteasome activity changes in LKB1 mutant tumors upon IFNγ stimulation. a, Real-time PCR showing antigen presentation genes expressing in LKB1 mutant lines with LKB1 overexpression. Left, H460 human NSCLC cells. Right, mouse KL cells with or without LKB1 over-expression. n = 3 experiments each group. (mean ± sd, unpaired *t* test, two tailed). $^{*}P < 0.05$, $^{***}P < 0.001$. **b**, Western blot showing immunoproteasome subunits PSMB9 and PSMB8 levels, TAP1, Tapasin and B2M expression (Upper panel) and conventional proteasome subunits PSMB5 and PSMB6 expression (lower panel) from KP or KL lung nodules. Samples are derived from the same experiment and blots were processed in parallel. Blots are cropped and uncropped images can be found in Source Data. **c**, KL Ulk1 shRNA cell lines (upper panel) and KP Ulk1 shRNA cell lines (lower panel) were stimulated with IFN γ (10 ng/ml) for 24 hrs before the measurement of immunoproteasome activities showed as relative fluorescent units (RFU) per min (Vmax). n = 3 cell cultures for each group. (mean ± sd, multiple two-sided unpaired *t* test, two-stage step-up method of Benjamini, Krieger and Yekutieli). **d**, Immunoproteasome cleavage activity corresponding to indicated substrate for two KLP cells (KLP T1 and KLP T2) after IFNγ stimulation shown as Vmax fold change compared with KL vehicle control group. n = 3 cell cultures each group. (mean ± sd, two-sided unpaired multiple *t* test, two-stage step-up method of Benjamini, Krieger and Yekutieli). **e**, Immunoproteasome activity for KL (left) and H460 (right) with or without LKB1 over-expression. n = 3 cell cultures each group. (mean ± sd, two-sided unpaired multiple *t* test, two-stage step-up method of Benjamini, Krieger and Yekutieli).

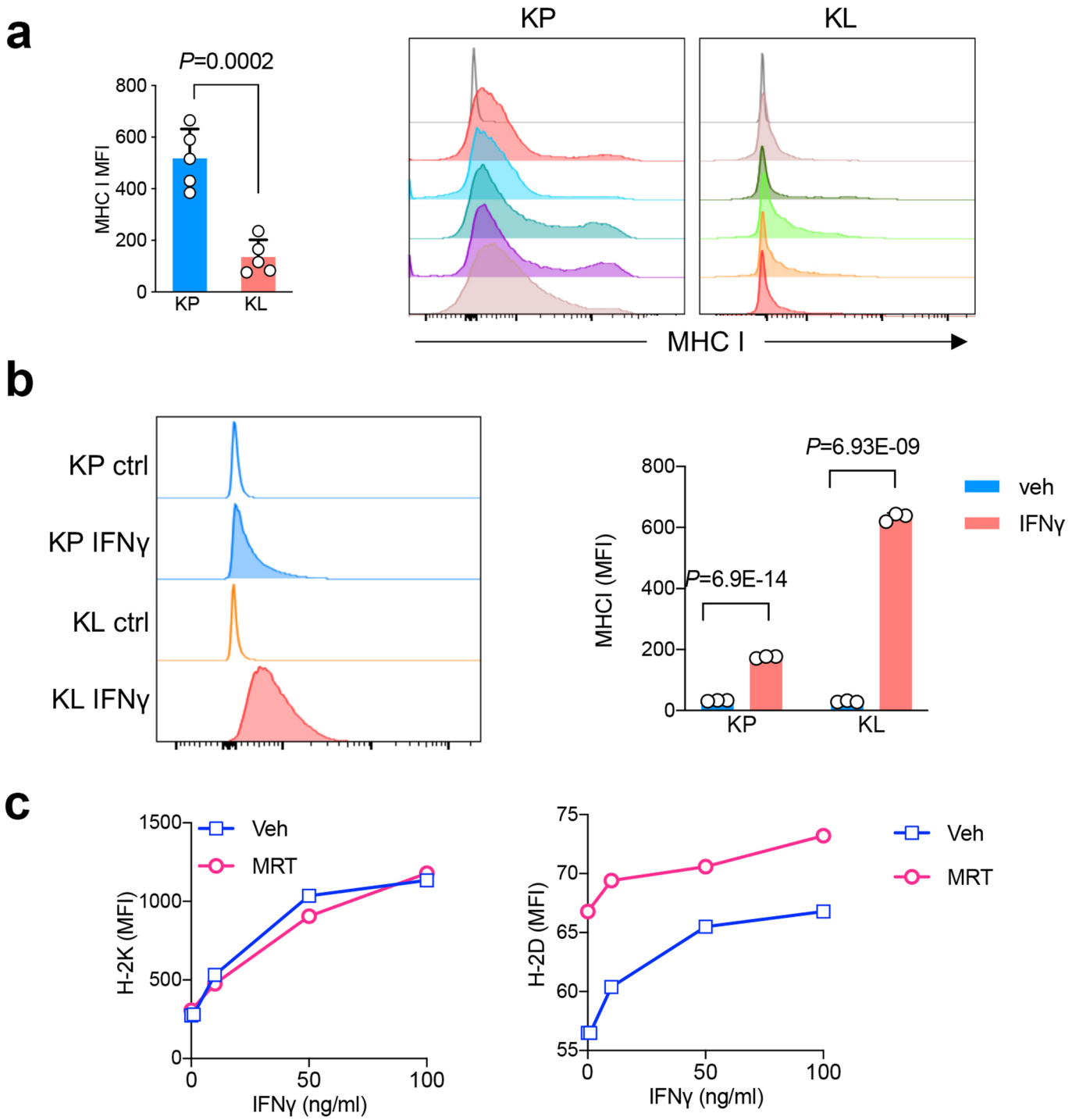

Extended Data Fig. 5 | MHCI levels in KL and KP tumors. a, MHCI levels from KP or KL allograft tumors as quantified as median fluorescent intensity (MFI) (left). Right, representative histograms depict MHCI level from mice with KP and KL tumors. n = 5 tumors each group. (mean ± sd, two-sided *t* test, unpaired) **b**, MHCI levels from KP or KL tumor cell lines stimulated with IFNγ as shown MFI levels. Left panel, representative histograms. Right panel, quantification of MHC I expression levels in KP and KL after IFNγ (100 ng/ml) stimulation for 18 hrs. n = 3 cell cultures each group. Shown representative result of three independent experiments (mean ± sd, multiple *t* test, FDR < 0.05). **c**, MHC I subunit H-2K and H-2D levels change in response to ULK1 inhibitor MRT68921 in mouse KL line *in vitro* 48hrs after the treatment. Data representative of two independent experiments.

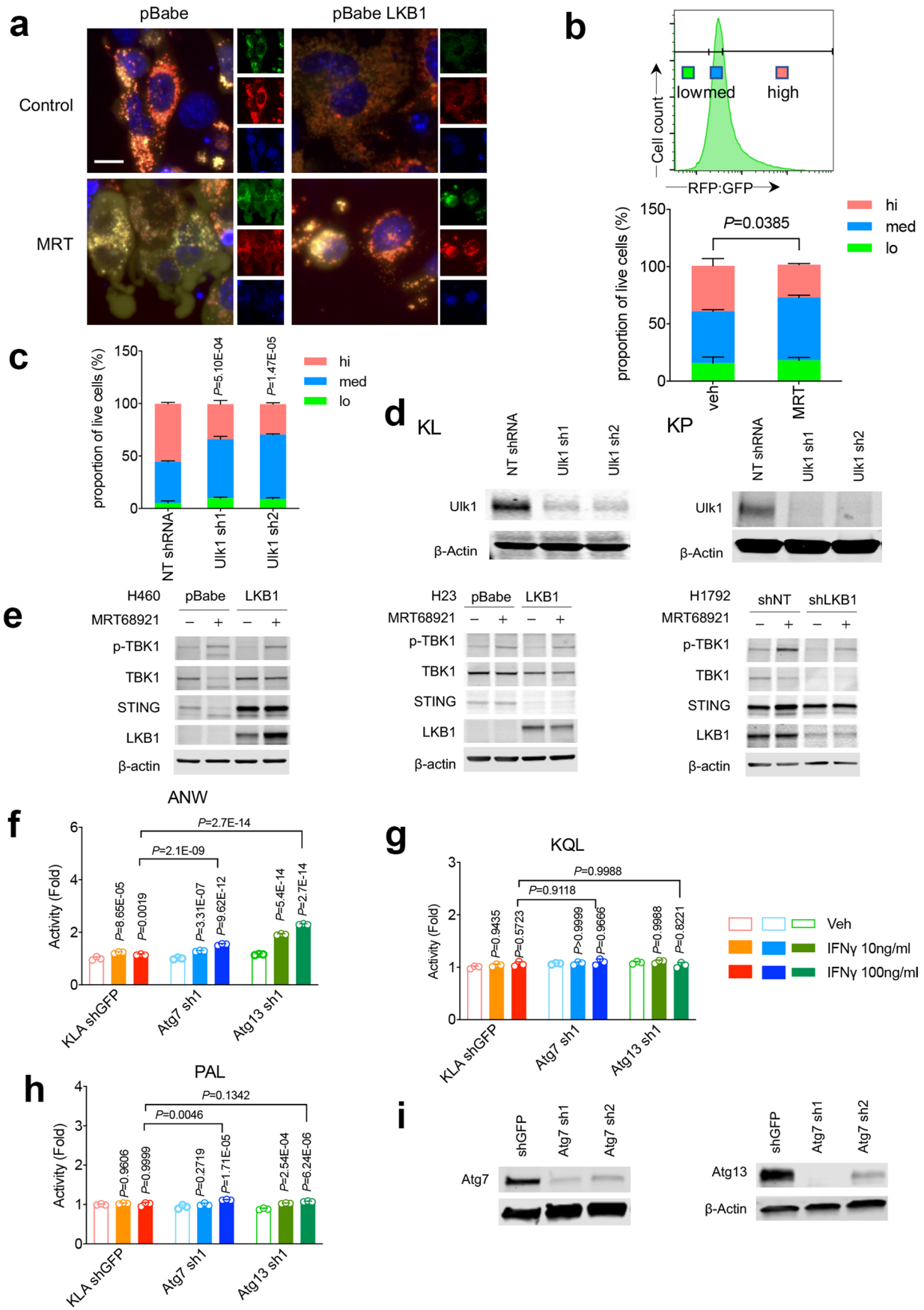

Extended Data Fig. 6 | See next page for caption.

Extended Data Fig. 6 | Targeting autophagy pathway in LKB1 mutant NSCLC tumors. a, Representative immunofluorescent (IF) image of autophagy flux in KL and KL-LKB1 tumor cells in response to MRT using GFP-mCherry-LC3B reporter. Red, GFP-mCherry+ LC3 puncta; yellow, GFP + mCherry+ puncta. scale bar, 15 μm. Data representative of 2 independent experiments. **b**, Quantification of autophagic flux by GFP-RFP-LC3 reporter in KL tumors treated with MRT as left using flow cytometry analysis. Upper panel, gating strategy. Lower panel, quantification of autophagic flux shown as RFP:GFP ratios. n = 3 cell cultures each group. Data shown represents one of three independent experiments (mean ± sd, two-tailed *t* test for high group, unpaired). **c**, Quantification of autophagic flux ratio (RFP:GFP) in KL cells with GFP-RFP-LC3 reporter transduced with Ulk1 shRNA. n = 3 cell cultures each group. Data shown one of two independent experiments. (mean ± sd, two-tailed *t* test for high group, unpaired). Samples were compared with NT shRNA cells for high group. **d**. western blot showing ULK1 protein levels in KL (left) and KP (right) stable cell lines with *Ulk1* shRNA. Data represents one of two independent experiments. **e**, Western blot of ULK inhibitor MRT68921 in human LKB1 isogenic lines for TBK1/STING pathway changes of H460 (left) and H23 (middle) and H1792 (right). Data represents one of two independent experiments. **f**,**g**,**h**, Immunoproteasome activity for KL stable cell lines with Atg7 or Atg13 for ANW (**f**), KQL (**g**) or PAL (**h**) substrate. n = 3 independent experimental samples for each group. (data presented are shown as mean±sd, two-sided one-way ANOVA, Tukey test, statistics presented on top of each column is compared with vehicle group, and pairwise comparisons between groups after 100 ng/ml IFNγ treatment shown on top of columns). Data shown one of two independent experiments. **i**, Western blot of KL stable cell lines generated with either Atg7 shRNA (left panel) or Atg13 shRNA (right panel). Shown one of two independent experiments. Blots in panels d, e and i are cropped and uncropped images can be found in Source Data.

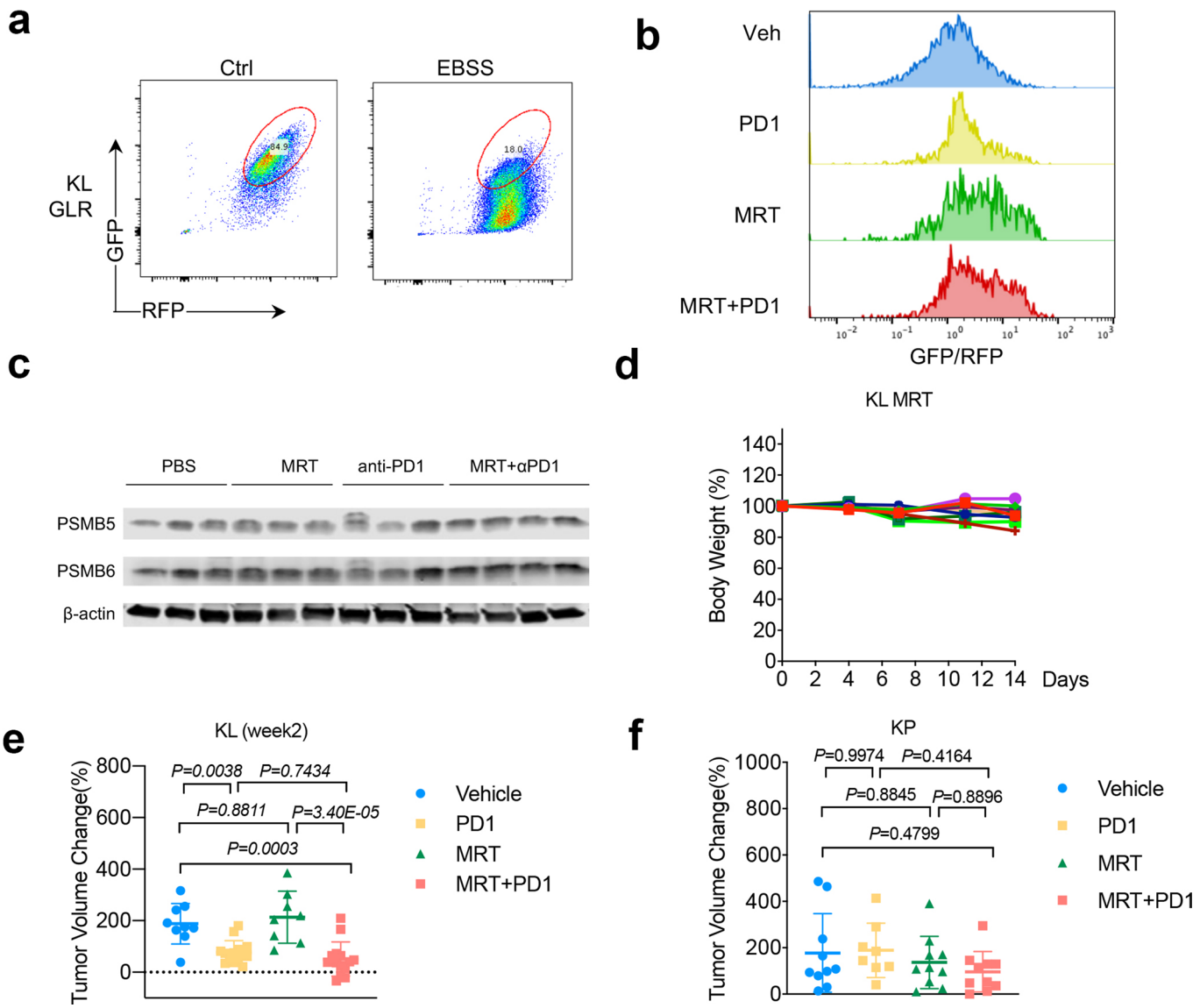

Extended Data Fig. 7 | Targeting autophagy in LKB1 mutant NSCLC tumors in vivo. a, validation of KL cells transduced with autophagy flux reporter GFP–LC3-RFP (GLR). Generated KL GLR cells were starved in EBSS buffer for 24 hrs before FACS analysis for RFP/GFP signals. **b**, Representative FACS analysis of GFP/RFP ratio of KL tumors after indicated treatments. Data representative of 2 independent experiments. **c**, Western blot shows conventional proteasome subunits PSMB5 and PSMB6 expression levels from KL lung nodules after MRT + PD1 treatment. Each lane represents one individual mouse tumor nodule. **d**, Toxicity of MRT68921 shown as mouse body weight change percentage after the drug treatment. Each line represents one mouse. n = 9. **e**, Tumor volume changes after 2-week treatment of KL GEMM tumors with MRT + PD1. Veh n = 9, PD1 n = 14, MRT n = 8, MRT + PD1, n = 14 tumors each group. (mean ± sd, one-way ANOVA). **f**, Tumor volume change of KP allograft tumor 1 week after indicated treatment. Veh, MRT, MRT + PD1 n = 10; PD1 n = 8 tumors each group. (mean ± sd, one-way ANOVA).

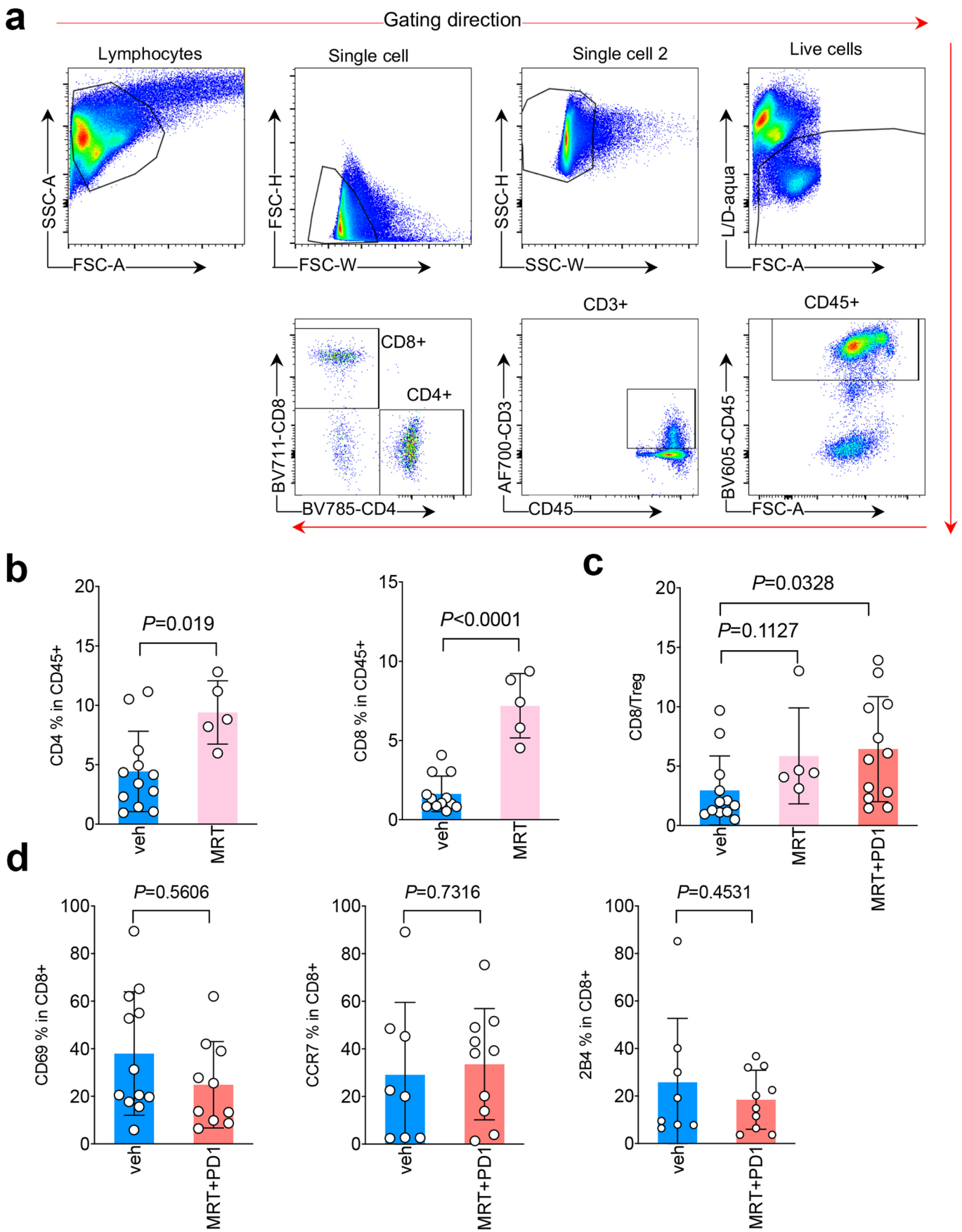

Extended Data Fig. 8 | See next page for caption.

Extended Data Fig. 8 | Immune infiltrates analysis in KL tumors after ULK1 inhibitor treatment. a, Gating strategy used for immune analysis. **b**, FACS analysis of CD4 + (left) and CD8 + (right) T lymphocytes among total tumor infiltrating CD45 + leukocytes in KL tumor after the treatment of ULK1 inhibitor MRT68921 (MRT). Veh n = 12, MRT n = 5 tumors each group. (mean ± sd, unpaired *t* test, two tailed). **c**, CD8/Treg ratio of total tumor infiltrating leukocytes (TILs) after the indicated drugs treatment. veh n = 12, MRT n = 5, MRT + PD1 n = 12 tumors each group. (mean ± sd, unpaired *t* test, two tailed). **d**, CD69, CCR7 and 2B4 levels within CD8 + T cells after MRT68921 (MRT) and anti-PD1 treatment. Left panel, veh n = 12, MRT + PD1 n = 10. Middle and right panel, veh n = 8, MRT + PD1 n = 10 tumors each group. (mean ± sd, unpaired *t* test, two tailed.).